Master's Thesis

Czech
Technical
University
in Prague

F4

Faculty of Nuclear Sciences and Physical Engineering
Department of Physics

Development of a new runaway electron diagnostics method based on strip semiconductor detectors

Bc. Marek Tunkl

Supervisor: Ing. Michal Marčišovský, Ph.D.
Field of study: Physics and Technology of Thermonuclear Fusion
May 2022

ČESKÉ VYSOKÉ UČENÍ TECHNICKÉ V PRAZE
FAKULTA JADERNÁ A FYZIKÁLNĚ INŽENÝRSKÁ
PRAHA 1 - STARÉ MĚSTO, BŘEHOVÁ 7 - PSČ 115 19

Katedra: fyziky *Akademický rok:* 2020/2021

ZADÁNÍ DIPLOMOVÉ PRÁCE

Student: Bc. Marek Tunkl

Studijní program: Aplikace přírodních věd

Obor: Fyzika a technika termojaderné fúze

Název práce: (česky) Vývoj nové diagnostiky ubíhajících elektronů na bázi křemíkových stripových detektorů

Název práce: (anglicky) Development of a new runaway electron diagnostics method based on strip semiconductor detectors

Pokyny pro vypracování:

1) Fyzika termojaderné fúze, tokamak GOLEM
2) Ubíhající elektrony a jejich vznik a charakteristika
3) Polovodičové a scintilační detektory ionizujícího záření
4) Vývoj detekční instrumentace pro detekci ubíhajících elektronů
5) Analýza experimentálních dat a srovnání s existujícími metodami diagnostiky

Doporučená literatura:

[1] P. Kulhánek: Úvod do teorie plazmatu, AGA, 2011

[2] J. Wesson: Tokamaks, Oxfor University Press, 2011

[3] G. F. Knoll: Radiation Detection and Measurement, Wiley, 2010

[4] G. Lutz: Semiconductor Radiation Detectors, Springer, 1999

[5] K. Iniewski: Radiation Effects in Semiconductors, CRC Press, 2011

Jméno a pracoviště vedoucího diplomové práce:

Ing. Michal Marčišovský, Ph.D., Katedra fyziky,
Fakulta jaderná a fyzikálně inženýrská ČVUT v Praze

Datum zadání diplomové práce: 23.10.2020

Termín odevzdání diplomové práce: 03.05.2021

Doba platnosti zadání je dva roky od data zadání.

.....
garant oboru

.....
vedoucí katedry

.....
děkan

ČESKÉ VYSOKÉ UČENÍ TECHNICKÉ V PRAZE
Fakulta jaderná a fyzikálně inženýrská
-1-

V Praze dne 23.10.2020

Acknowledgements

First of all, I want to express my sincere thanks to my parents and my sister for their support and motivation. Without their help this work would not exist. Also, I would like to express my deepest appreciation to my supervisor Ing. Michal Marčišovský, Ph.D. for his insightful comments and expert advice, without which this thesis would not have been possible. I am also grateful to the Ing. Vojtěch Svoboda, CSc. for the support and for the opportunity to operate on the GOLEM tokamak. My thanks also belong to my colleague, Ing. Sergei Kulkov, for language revisions.

Declaration

Prohlašuji, že jsem svou diplomovou práci vypracoval samostatně a použil jsem podkladky (literaturu, projekty, SW, atd...) uvedené v přiloženém seznamu.

Nemám závažný důvod proti použití tohoto školního díla ve smyslu §60 Zákona č. 121/2000 Sb., o právu autorském, o právech souvisejících s právem autorským a změně některých zákonů (autorský zákon).

V Praze dne ....

podpis

Abstract

In this master's thesis, new diagnostics of runaway electrons on the GOLEM tokamak were developed. First, a simulation in the Geant4 toolkit was created to evaluate the effect of the backscattering of the runaway electrons from the limiter. Then, a silicon-based strip detector probe was designed and constructed with respect to the simulation result. Finally, the measured data were analyzed and compared to the relevant diagnostics and simulation results. Furthermore, a new scintillation detector was constructed from a silicon photomultiplier and a LYSO crystal. The signal from the silicon photomultiplier exhibited good characteristics. Even with multiple superimposed peaks, it was possible to reconstruct their original height and thus obtain the hard X-ray spectrum of the entire plasma discharge.

Keywords: LYSO, PH32, semiconductor detector, silicon photomultiplier, tokamak, runaway electrons

Supervisor: Ing. Michal Marčišovský, Ph.D.
Katedra fyziky,
Fakulta jaderná a fyzikálně inženýrská
ČVUT v Praze

Abstrakt

Tato diplomová práce se zabývá vývojem nové diagnostiky unikajících elektronů na tokamaku GOLEM. Nejprve byla vytvořena simulace v toolkitu Geant4, ve které byl studován vliv zpětného rozptylu ubíhajících elektronů na limiteru. Poté byla s ohledem na výsledek simulace navržena a zkonstruována sonda s křemíkovým stripovými detektory. Naměřená data byla porovnána s relevantními diagnostikami a výsledky simulace. Dále byl sestaven nový scintilační detektor z křemíkového fotonásobiče a LYSO krystalu. Signál z křemíkového fotonásobiče vykazoval dobré vlastnosti. Dokonce i při vícenásobném překrytí píků bylo možné rekonstruovat jejich původní výšku a získat tak tvrdé spektrum rentgenového záření z celého výboje.

Klíčová slova: křemíkový fotonásobič, LYSO, PH32, polovodičový detektor, tokamak, ubíhající elektrony

Překlad názvu: Vývoj diagnostiky ubíhajících elektronů na bázi křemíkových stripových detektrorů

Contents

Introduction **1**

1 Thermonuclear fusion **3**
1.1 Plasma 4
1.2 Charged particle motion in an electric and magnetic field 5

2 Tokamak **7**
2.1 Magnetic fields 8
2.2 Particle orbits in tokamak magnetic field 10
2.3 GOLEM tokamak 11

3 Runaway electrons **13**
3.1 Generation of runaway electrons 13
3.1.1 Primary (Dreicer's) mechanism 14
3.1.2 Hot tail mechanism 16
3.1.3 Secondary mechanism 16
3.2 Mitigation of Runaway electrons (REs) 17
3.3 Runaway orbits 17
3.4 Radiation loses 18
3.4.1 Bremsstrahlung 18
3.4.2 Synchrotron radiation 18
3.5 Diagnostics for RE 18

4 Interaction of ionizing radiation with solid matter **21**
4.1 Interaction of fast electrons 21
4.2 Interaction of X-ray radiation . . 22
4.2.1 Photoelectric absorption 22
4.2.2 Compton scattering 23
4.2.3 Pair production 23

5 Semiconductor detectors **25**
5.1 Properties of semiconductors . . . 25
5.2 Extrinsic semiconductors 26
5.3 *p-n* junction 26
5.4 The strip detector with PH32 ASIC 28
5.4.1 Sensor 28
5.4.2 PH32 readout chip 28

6 Scintillation detectors **33**
6.1 Scintillators 33
6.1.1 Inorganic scintillators 34
6.1.2 Organic scintillators 34
6.2 Photodetectors 34
6.2.1 Photomultiplier tube 34
6.2.2 Silicon photomultiplier 35

7 Monte Carlo particle transport simulations **37**
7.1 Geant4 37
7.1.1 Physics list 38
7.1.2 Geometry 38
7.1.3 Magnetic Field 38
7.2 Strip detector model 38
7.2.1 Strip detector setups 39
7.3 World models 39
7.3.1 Linear model 40
7.3.2 Simplified tokamak model . . . 40

8 Results **43**
8.1 Geant4 simulations 43
8.1.1 Backscattering in a magnetic field 43
8.1.2 Strip detector response to REs 44
8.2 Experiments on GOLEM tokamak 46
8.2.1 Setup 46
8.2.2 Hard X-ray (HXR) spectractrum reconstruction 47
8.2.3 Strip detector 48

Conclusion **57**

Bibliography **59**

Acronyms **63**

Figures

1.1 The dependence of the cross-section of DT and DD reaction on temperature 4

2.1 Tokamak schematics 7
2.2 Schematic cross-section of limited and diverted plasma 9
2.3 Magnetic flux surfaces 10
2.4 Trapped particle orbit 11

3.1 Momentum-dependent friction force 14

4.1 Interactions of γ radiation 22
4.2 A diagram of Compton scattering 23

5.1 Effects of semiconductor dopants 27
5.2 The schematics of p-n junction . 27
5.3 The 32-strip silicon detector with PH32v8 chip 28
5.4 The cross-section of sensor 29
5.5 Diagram of the analog part of the ASIC detector PH32 30
5.6 Principle of signal processing in a PH32 chip 31

6.1 A schematic of a scintillator detector with PMT 34
6.2 Silicon photomultiplier and one microcell schematics 35

7.1 The GDML model of PH32 strip detector 39
7.2 The GDML models of different PH32 setups 40
7.3 The GDML model for backscattering studies 41
7.4 Simplified GDML model of the tokamak. 41

8.1 Geant4 simulations of REs backscatering 44
8.2 The Gean4 simulation of strip detector response to REs 45
8.3 Experimental setup 46
8.4 Photos of setup with two strip detectors mounted on the manipulator 47
8.5 U_{loop}, I_{p} and RE drift $v_{\mathrm{drift}}(a)$ estimate 47
8.6 #37150 waveforms from HXR probes 48
8.7 Expected response of detetor . . . 49
8.8 Shot #38514 50
8.9 Shot #38289 51
8.10 Shot #38290 51
8.11 Shot #38503 53
8.12 Shot #38509 54
8.13 Shot #38952 55

Introduction

The beginning of thermonuclear fusion research can be traced back to a prophet-like statement from Arthur Eddington:

"If, indeed, the sub-atomic energy in the stars is being freely used to maintain their great furnaces, it seems to bring a little nearer to fulfilment our dream of controlling this latent power for the well-being of the human race – or for its suicide." [1]

This is a quote from his speech "Internal Constitution of the Stars", where he proposed that mass defect between four hydrogen atoms and a helium atom along with equivalency of mass and energy (now known even to the general public in a form of equation $E = mc^2$) shows that the source of solar energy is thermonuclear fusion.

Unfortunately, regarding this quote, we started from the grimmer end. The first demonstration of thermonuclear fusion on earth was in November 1952 the thermonuclear bomb *Ivy-Mike* [2]. Now, 70 years later the works on the large thermonuclear reactor, the tokamak ITER, are coming to an end. This device will hold the hot plasma in a magnetic cage long enough for a thermonuclear reaction to occur. The first plasma operation is planned in 2031 and in 2041 the reactor should achieve full power and demonstrate that thermonuclear fusion power is a feasible source of energy.

Even though the construction is in progress, all the problems regarding plasma confinement are not yet fully solved. During the plasma discharge, plasma can exhibit unstable behavior. These instabilities can even pose threat to the tokamak device and should be avoided. One of these instabilities disruptions, events characterized by a sudden loss of confinement. During a disruption, there can occur a rampant acceleration of plasma electrons, which can gain relativistic energies. These highly energetic electrons are called REs. When REs are expelled from the plasma, they can pose a serious threat to the plasma-facing components (PFC) at localized spots and reduce the lifetime of the tokamak wall or destroy the sensitive diagnostics. Therefore, the understanding of physics governing REs and methods of their avoidance and mitigation is of great importance for future tokamak fusion reactors.

The GOLEM tokamak is a small tokamak device located at Faculty of Nuclear Sciences and Physical Engineering (FNSPE). It is used mostly for the education of future fusion scientists and as a testbed for new diagnostics

development. Because of its plasma parameters REs are present in a almost every discharge.

Semiconductor particle detectors are commonly used in high-energy particle physics experiments. Their uses are now broadening and now also include the diagnostics of REs. Integration of semiconductor strip and pixel detectors is a somewhat novel approach in plasma diagnostics and they need to be adapted for operation in the tokamak environment.

Independently on this notion, the new type of semiconductor-based photodetectors the Silicon Photomultipliers (SiPMs) are progressively replacing conventional Photomultiplier Tubes (PMTs) tubes in many applications like medicine, particle physics, and astronomy.

Building on previous work of [3, 4] a new strip semiconductor detector assembly was developed and used at GOLEM tokamak to investigate the effect of RE interaction with the tokamak vessels, as part of this thesis, And a Lutetium Yttrium Orthosilicate (LYSO) scintillation crystal coupled with SiPM has been added to the HXR diagnostics setup at GOLEM tokamak.

The body of this thesis starts with an introduction to the fundamentals of thermonuclear fusion, plasma physics, and tokamak devices. The second chapter presents the physics of REs, the mechanism of their generation, their orbits and radiation, and diagnostics methods are described and, lastly, mechanisms of their mitigation are outlined. The next chapter is dedicated to the interaction of ionizing radiation with matter, relevant for RE diagnostics. The fifth and sixth chapters present the semiconductor and scintillation detectors. The seventh chapter describes the Geant4 simulation toolkit and the models used to simulate a RE interaction in tokamak and with the strip detector. Finally, in the eighth chapter, the result of simulations and measurements on GOLEM tokamak are presented.

Chapter 1

Thermonuclear fusion

Nuclear fusion is a nuclear reaction of atom nuclei during which energy is released. The reaction of two protons producing deuterium, like the one that occurs in the core of the Sun, is governed by weak interaction and has a relatively small cross-section. Thus it is not suitable for terrestrial energy production. The least difficult fusion reaction to sustain is the deuterium-tritium reaction (DT), which has the highest reactivity at temperatures around $2 \cdot 10^8\,°\mathrm{C}$.

Since the 1930s, the scientific community has been trying to design a fusion reactor to generate energy. The methods for achieving this goal have evolved, but most of the proposed solutions for fusion reactors use DT fuel. Apart from the DT reaction, DD synthesis will also naturally occur in a fusion reactor, but its contribution to fusion power would be minor. The reactions of interest are:

$$ {}^{2}_{1}\mathrm{D} + {}^{3}_{1}\mathrm{T} \rightarrow {}^{4}_{2}\mathrm{He}\ (3.5\,\mathrm{MeV}) + {}^{1}_{0}\mathrm{n}\ (14.1\,\mathrm{MeV}), \tag{1.1} $$

$$ {}^{2}_{1}\mathrm{D} + {}^{2}_{1}\mathrm{D} \rightarrow {}^{3}_{1}\mathrm{T}\ (1\,\mathrm{MeV}) + {}^{1}_{1}\mathrm{p}\ (3\,\mathrm{MeV}), \tag{1.2} $$

$$ {}^{2}_{1}\mathrm{D} + {}^{2}_{1}\mathrm{D} \rightarrow {}^{4}_{2}\mathrm{He}\ (0.8\,\mathrm{MeV}) + {}^{1}_{0}\mathrm{n}\ (2.5\,\mathrm{MeV}). \tag{1.3} $$

The cross-section of the DT reaction as a function of temperature is shown in figure 1.1. It will be necessary to sustain temperatures around ten keV in a fusion power plant. The DT mixture will be fully ionized and in the plasma state at this temperature.

Deuterium has a high natural abundance; approximately 0.02 % of naturally occurring hydrogen in water are deuterons; thus it could be harvested from oceans. For production of 1 GW electric power per day, only 1 kg of deuterium is needed [5]. This amount can be harvested from $25\,\mathrm{m}^3$ of water. A majority of which will be left to other possible uses. However, tritium has a short half-time of approximately 12.32 years, and therefore it can not be naturally harvested and must be prepared artificially by nuclear reactions. Nevertheless, tritium could be directly generated on-site in a future fusion reactor, taking advantage of nuclear reactions between the fusion-generated neutrons and lithium in breeding blankets.

The requirement for achieving fusion DT is called triple product $nT\tau_\mathrm{E}$. The triple product consists of three parameters: n is the fuel density, is T the temperature, and τ_E is the energy confinement time, the measure of system

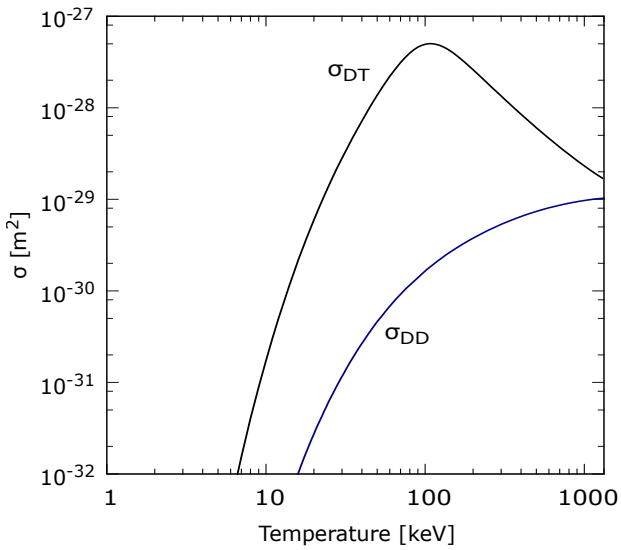

Figure 1.1: The dependence of the cross-section of DT reaction and the total cross-section of both DD reactions on the temperature in keV (1 eV corresponds to approximately 11 700 K) [5].

energy loss. When the product of these three parameters is above a certain threshold, fusion reactions will produce more power than is needed to sustain them, releasing net energy. The triple product has a minimum at $T = 14\,\mathrm{keV}$ for DT reactions, approximately ten times the temperature at the Sun's core. The triple product condition takes the form:

$$nT\tau_{\mathrm{E}} \geq 3 \cdot 10^{21}\,\mathrm{keV} \cdot \mathrm{s} \cdot \mathrm{m}^{-3}. \tag{1.4}$$

Maximizing all three plasma parameters in (1.4) is hard to achieve. There are two primary branches of fusion research: Inertial Confinement Fusion (ICF) and Magnetic Confinement Fusion (MCF). In ICF, high-energy lasers achieve high densities and temperatures by compressing a frozen pellet made of the DT mixture. The MCF uses magnetic fields to confine plasma at a lower density but for a longer time.

1.1 Plasma

"A plasma is a quasineutral gas of charged and neutral particles which exhibits collective behavior" [6]. A macroscopic volume seems neutral in quasi-neutral gas, even though it contains charged particles. In plasma, the electric potential of inserted charged particle is shielded to 1/e of its original value at the

distance of Debye length defined as:

$$\lambda_{\mathrm{D}} = \sqrt{\frac{\varepsilon_0 k_{\mathrm{B}} T}{n_{\mathrm{e}} e^2}}, \tag{1.5}$$

where ε_0 is the vacuum permittivity, k_{B} is the Boltzmann constant and e, T_{e} are electric charge and temperature of electrons in the plasma and n is the plasma density [5].

The Coulomb interaction between charged particles has a more extended range than the binary collision. Because of this fact, we talk about the collective behavior of the plasma.

1.2 Charged particle motion in an electric and magnetic field

Charged particle motion is influenced by the Lorentz force. The equation of motion for charged particle in electric $\mathbf{E}$ and magnetic $\mathbf{B}$ field has the following form

$$m\frac{\mathrm{d}\mathbf{v}}{\mathrm{d}t} = q(\mathbf{E} + \mathbf{v} \times \mathbf{B}), \tag{1.6}$$

where q and $\mathbf{v}$ are particle charge and velocity, respectively. A magnetic field curves a particle trajectory dependent on velocity $v_\perp$ perpendicular to the magnetic field. The magnetic field does not affect the particle movement in the longitudinal direction. $\mathbf{B}$ will make the particle follow a circular motion around magnetic field lines with frequency ω_c and radius r_L. This motion is called Larmor rotation. The scales of Larmor rotation are given by

$$\omega_{\mathrm{c}} = \frac{qB}{m}, \quad r_{\mathrm{L}} = \frac{mv_\perp}{qB}, \tag{1.7}$$

where B is magnetic field, m particle mass and q its charge.

Energy of runaway electron can reach the orders of keV, when its energy becomes comparable to the electron rest mass $m_{\mathrm{e}} \doteq 511\,\mathrm{keV/c^2}$. The relativistic description of motion is provided by modified version of (1.6) in the following form

$$\frac{\mathrm{d}}{\mathrm{d}t}(m_0\gamma\mathbf{v}) = q(\mathbf{E} + \mathbf{v} \times \mathbf{B}), \tag{1.8}$$

where m_0 represents the rest mass of particle and $\gamma = \frac{1}{\sqrt{1-\frac{v^2}{c^2}}}$ is the Lorentz factor. Equations for Larmor radius and cyclotron frequency are similar, while m is replaced by $m_0\gamma$.

Particle drifts

Particles in an arbitrarily complex configuration of an electric and magnetic field can be described by (1.6). But in slowly varying magnetic and electric fields the description of particle movement can be simplified to Larmor rotation around the so-called guiding center which exhibits the following drifts [5]:

$\mathbf{E} \times \mathbf{B}$ drift. In an environment with an electric and magnetic field the drift velocity of $\mathbf{E} \times \mathbf{B}$ is described by equation

$$\mathbf{v}_{\mathbf{E}\times\mathbf{B}} = \frac{\mathbf{E} \times \mathbf{B}}{B^2}. \tag{1.9}$$

This drift is independent of particle mass and charge, thus this drift causes the flux of charged particles in the plasma.

Curvature drift. One of the drifts caused by the non-uniformity of the magnetic field is the curvature drift. This drift has the velocity

$$\mathbf{v}_{\mathrm{R}} = \frac{m v_{\parallel}^2}{q B R_{\mathrm{c}}} \mathbf{R}_{\mathrm{c}} \times \mathbf{B}. \tag{1.10}$$

The $\mathbf{R}_{\mathrm{c}}$ denotes the radius of curvature and $v_{\parallel}$ component of velocity parallel to the magnetic field line.

grad-B drift. Non-uniformity of magnetic flux strength results in a so-called grad-B drift. It often accompanies the curvature drift.

$$\mathbf{v}_{\boldsymbol{\nabla}\mathrm{B}} = \frac{v_{\perp} r_{\mathrm{L}}}{2B^2} \mathbf{B} \times \boldsymbol{\nabla} B. \tag{1.11}$$

As before, it has a dependence on charge and the same direction. These two drifts lead to charge separation in the plasma.

Polarization drift. From the slow variation of electric field arises polarization drift, this leads to change of $\mathbf{E} \times \mathbf{B}$ drift and results in drift with velocity

$$\mathbf{v}_{\mathrm{p}} = -\frac{1}{\omega_{\mathrm{c}} B} \frac{\mathrm{d}\mathbf{E}}{\mathrm{d}t}. \tag{1.12}$$

Particle motion modeling

The simplest particle motion model can be made by solving the Lorentz equation. This is called full orbit modeling. Another approach is guiding center modeling. This method relies on computing the guiding center motion rather than the modeling of the whole particle trajectory.

Because the motion of a charged particle in an electric field is governed by multiple time scales: fast gyromotion and slow guiding center drifts, a choice of the numerical integrator is essential. For instance, while the standard 4th Runge-Kutta method (RK4) has a truncation error of 4th order, it fails to describe long timescales of particle dynamics [7]. For solving the Lorentz equation, the leap-frog method or Boris-Buneman algorithm is often used.

Chapter 2

Tokamak

The tokamak is currently the most promising design among magnetic confinement fusion devices. The name tokamak is an acronym for Russian "**to**roidal'naya **ka**mera s **ma**gnitnymi **k**atushkami" – toroidal vessel with magnetic coils. It is a device that confines the plasma in a torus-shaped vacuum vessel cage, with a magnetic field consisting of toroidal B_{t} and poloidal B_{p} components. Combining these fields results in the helical magnetic field, which confines the plasma inside the vacuum vessel. Three sets of coils are used for generating the confining magnetic field (see figure 2.1).

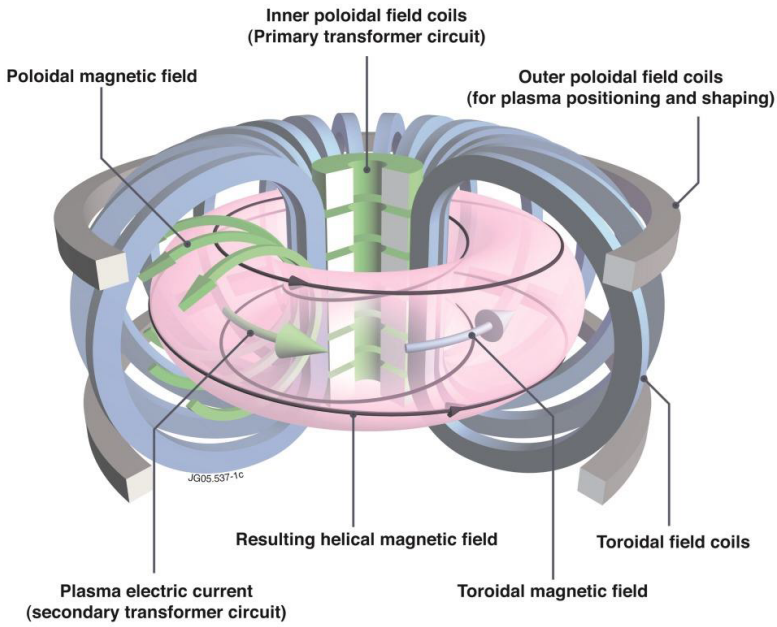

Figure 2.1: Tokamak schematics [5]. Toroidal field coils create the toroidal field, and magnetic flux from the central solenoid drives the plasma current, which results in the poloidal magnetic field. A combination of these two is a helical magnetic field confining the plasma.

First, toroidal field coils wrap around the vacuum vessel and create a magnetic field with intensity in order of several T.

The primary winding of the transformer in the tokamak center constitutes the second set of coils. Nowadays, it is often reduced to a central solenoid. It

induces an electric current in plasma I_p by a change of magnetic flux. The plasma thus behaves like the secondary winding of a transformer. Plasma current enables Ohmic heating of the plasma and, according to Ampère's, law generates a poloidal magnetic field B_p. The intensity of the poloidal magnetic field is an order of magnitude lower than of the toroidal one.

The third set of poloidal coils generates a vertical magnetic field B_v, which prevents toroidal magnetic configuration from expanding. These coils are accompanied by other windings that help shape the plasma. Older tokamaks operate with a circular plasma shape. Modern devices form plasma to a D shape.

At first, plasma is heated mainly via Joule heat generated from the plasma current. With growing plasma temperature, resistivity decreases, and Ohmic heating becomes ineffective. There are other means that can be used to heat the plasma. They include neutral beam injectors (NBI) and radio-frequency (RF) heating. The NBI system injects accelerated fuel atoms into the plasma. These atoms penetrate the magnetic confinement cage to the plasma center, where they become ionized and pass their energy to plasma.

RF heating systems operate at different radio frequencies, depending on which component of the plasma we want to energize: ionic cyclotron, down-hybrid, electron cyclotron frequency and their harmonics.

These non-inductive heating systems may even provide a non-inductive current drive. This allows bypassing plasma current generation by the change of magnetic flux via a central solenoid, which makes tokamak a pulse device by nature.

Impurities in the plasma radiate its energy and cool the plasma, thus they drastically reduce the parameters needed for achieving fusion. The tokamak vessel must be maintained in a high vacuum.

The plasma interaction with the vacuum vessel wall is presented with an obstacle limiting the plasma radius – the limiter. For even better separation between the plasma and Plasma Facing Comonent (PFC), the magnetic configuration is altered to contain X-point – the point where $B_\mathrm{p} = 0$. This is called divertor configuration. Configuration with a limiter and with a divertor is illustrated in figure 2.2.

In large tokamaks with longer discharge durations, the thermal loads are more extensive than any known material can sustain. In addition, it was discovered that in divertor configuration it is possible to achieve much better plasma parameters due to the formation of the transport barrier at the plasma edge. This mode is called H-mode because it enables higher confinement. Because of this, modern tokamaks switch to a divertor configuration during plasma discharge.

2.1 Magnetic fields

The strength of the toroidal magnetic field scales with the distance R from the tokamak center as $1/R$. The side closer to the tokamak center is referred to as High-Field Side (HFS), and the side farther is called Low-Field Side

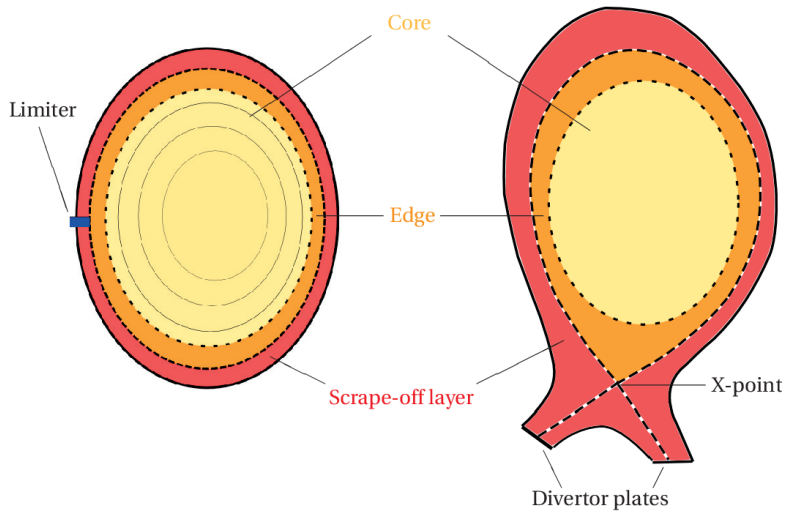

Figure 2.2: Schematic cross-section of limited plasma (left) and configuration with a divertor (right) [8].

(LFS). A toroidal magnetic field profile can is described as

$$B_{\mathrm{t}}(r) = \frac{r}{R} B_{\mathrm{t}}(0), \tag{2.1}$$

where r is the distance from the plasma center and R is the major device radius

Because the toroidal field is stronger, the resulting field lines have a small pitch angle. This angle is given as a dimensionless quantity called the safety factor q, which is defined as the number of turns in the toroidal direction required for the field line to make one full poloidal orbit. For the circular plasma, q has a form of

$$q = \frac{r}{R} \frac{B_{\mathrm{t}}}{B_{\mathrm{p}}(r)}. \tag{2.2}$$

The q is a function of the plasma radius. Typically, it has a minimum at the magnetic axis (typically $q(0) > 1$), and a maximum at the plasma edge where condition $q_{\mathrm{edge}} > 2$ should be satisfied, or plasma becomes unstable.

A magnetohydrodynamics (MHD) theory is used to describe magnetic field configuration in a tokamak. A condition for the stable plasma can be written as:

$$\boldsymbol{\nabla} p = \mathbf{j} \times \mathbf{B}, \tag{2.3}$$

where p is plasma pressure $\mathbf{j}$ plasma current and $\mathbf{B}$ confining magnetic field.

From this equation, it can be shown, that magnetic field lines lie on surfaces of constant magnetic flux (illustrated in the figure 2.4). Also, the pressure (therefore the temperature) is constant on these surfaces as the conditions

$$\mathbf{B} \cdot \boldsymbol{\nabla} p = 0, \qquad \mathbf{j} \cdot \boldsymbol{\nabla} p = 0 \tag{2.4}$$

are satisfied. The Last Closed Flux Surface (LCFS) is defined as the edge of the confined plasma. The region where flux surfaces are no longer closed

inside the tokamak is called a Scrape-Off Layer (SOL). If a particle leaves LCFS, it usually reaches the tokamak wall.

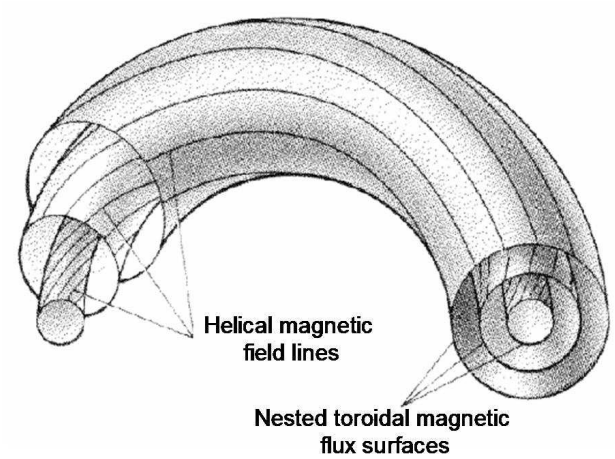

Figure 2.3: Magnetic field lines lies on magnetic flux surfaces. The surfaces are forming nested toroids [9]

Magnetic configuration is usually diagnosed by multiple coils and then reconstructed by Equilibrium Fitting (EFIT) algorithm. For a circular plasma, field profile can be derived from another plasma diagnostics, plasma current I_p: profile of circular tokamak plasma current density $j(r)$ can be described by equation

$$j(r) = \left[1 - \left(\frac{r}{a}\right)^2\right]^\nu, \tag{2.5}$$

where a is a minor tokamak radius and ν profile peaking factor [5]. From Ampère's law, the poloidal field profile is

$$B_\mathrm{p}(r) = \frac{\mu_0 j_0}{r} \int_0^r \rho \left[1 - \left(\frac{\rho}{a}\right)\right] \mathrm{d}\rho. \tag{2.6}$$

Which, after integration, gives

$$B_\mathrm{p}(r) = \frac{\mu_0 I_p}{2\pi r} \left[1 - (1 - \frac{r^2}{a^2})^{\nu+1}\right]. \tag{2.7}$$

From magnetic field strength B_t and plasma current I_p, a safety factor can be estimated as

$$q(r) = \frac{2\pi B_\mathrm{t}}{R\mu_0 I_\mathrm{p}} \cdot \frac{r^2}{1 - \left[1 - (\frac{r}{a})^2\right]^{\nu+1}}. \tag{2.8}$$

2.2 Particle orbits in tokamak magnetic field

The effects of the drift described in section 1.2 are overcome by the configuration of magnetic fields in a tokamak. The grad-B and curvature drifts

cause the vertical separation charge in the tokamak. This would result to $\mathbf{E} \times \mathbf{B}$ drift to LFS. It is prevented by effectively shorting the electric field by connecting the upper and lower part of plasma with curved magnetic field lines. It should be noted that in the SOL region, the magnetic field lines are not closed and drifts are present.

The typical particle follows a complete orbit around the magnetic surface. It is called a passing particle. Because of HFS and LFS strength change of toroidal magnetic field, a particle can be trapped on the LFS in a magnetic mirror. Because of the projection of trapped particle orbit to a poloidal plane, these particle orbits are called banana orbits.

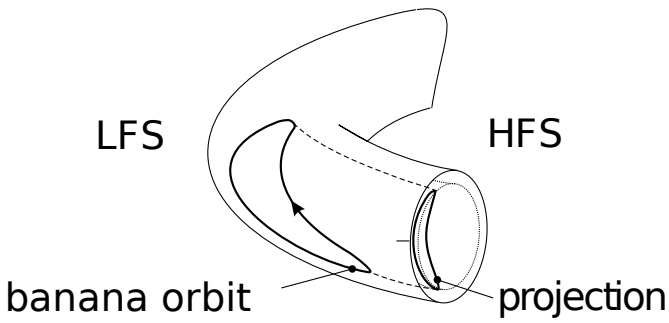

Figure 2.4: The schematics of a trapped particle orbit. Due to its shape it the poloidal projection, it is also called banana orbit, [9], modified

2.3 GOLEM tokamak

The GOLEM tokamak, which is located at the Faculty of Nuclear and Physical Engineering, is a small tokamak that serves primarily educational purposes. This small tokamak is one of the oldest tokamaks still in operation. Initially, the TM-1 tokamak (tokamak malyj - small tokamak) was build and operated in Kurchatov Institute since 1960s. In 1976 it was moved to the Institute of Plasma Physics of Czechoslovak Academy of Sciences for the study of the plasma-wall interactions and high-frequency waves plasma heating. After a significant upgrade — which included the new vacuum vessel and magnetic stabilization systems — its name was changed to CASTOR tokamak (Czech Academy of Sciences TORus). In 2007, it was retired and replaced by a larger COMPASS tokamak. Consequently, the former small tokamak was donated to the FNPSE, and it functions under the name GOLEM since 2009. The main parameters of the tokamak are summarized in table 2.1

GOLEM is a small tokamak with an iron transformer core and a circular cross-section of the vacuum chamber. A molybdenum limiter shapes the plasma. The chamber is made of stainless steel metal bellows with 0.2 mm thickness. There is a 10 mm thick copper shell around it. The toroidal field is driven by 28 copper coils, each wrapped in an aluminum casing. The tokamak

Major radius	$R_0 = 0.4\,\mathrm{m}$
Liner minor radius	$r_0 = 0.1\,\mathrm{m}$
Minor (limiter) radius	$a = 0.085\,\mathrm{m}$
Toroidal magnetic field	$B_\mathrm{t} < 0.8\,\mathrm{T}$
Plasma current	$I_\mathrm{p} < 8\,\mathrm{kA}$
Discharge duration	$\tau \approx 15\,\mathrm{ms}$
Plasma density	$n_\mathrm{e} \approx 1 \cdot 10^{18}\,\mathrm{m}^{-3}$
Effective charge of plasma	$Z_\mathrm{eff} \geq 2.5$

Table 2.1: The principal parameters of tokamak GOLEM [10]. The effective charge is usually assumed 2.5, but [11] suggest $Z_\mathrm{eff} \approx 5$ at minimum.

chamber has diagnostic 18 ports in the form of four small crosses and two big crosses. Each cross consists of two vertical posts (upper and lower) and one LFS port.

Four basic diagnostics are in operation during each discharge: loop voltage U_loop, toroidal magnetic field B_t, plasma current I_p and visible electromagnetic radiation.

To employ the tokamak for the education of international students it can be operated remotely via a web interface [12][1]. Other advantages of the GOLEM tokamak include the short time delay between discharges. In addition, plasma discharges at the tokamak can be easily performed with the plasma current and the toroidal magnetic field either in clockwise or anticlockwise directions.

[1]The discharge database is available online on `http://golem.fjfi.cvut.cz/shots/0/`. All raw data measurements presented in the result section can be found there.

Chapter 3

Runaway electrons

The runaway effect was probably first observed by Wilson [13] in 1925. This effect is not limited to thermonuclear plasmas only. It can play a role in explaining astrophysical and atmospheric phenomena. The runaway effect is a consequence of a decline of frictional force caused by Coulomb interactions in plasma at thermal and supra-thermal velocities. Thus the free acceleration of plasma particles above specific energy when an external force usually caused by an electric field occurs [1]. This effect can lead to the creation of a runaway electron population in a tokamak plasma.

3.1 Generation of runaway electrons

In the tokamak, there is always an electric field $\mathbf{E}$ driving the plasma current. Thus, an electron in the plasma is accelerated by a force

$$\mathbf{F}_{\mathrm{e}} = -e\mathbf{E}. \tag{3.1}$$

The Coulomb interactions with plasma ions and electrons result in a drag force usually formulated in the form:

$$\mathbf{F}_{\mathrm{d}} = -m_{\mathrm{e}}\nu_{\mathrm{coll}}(v)\mathbf{v}, \tag{3.2}$$

where m_{e} is the electron mass, $\mathbf{v}$ is the electron velocity against the bulk electrons and ions, and $\nu_{\mathrm{coll}}(v)$ is the collisional frequency with the plasma.

It is also possible to derive the collisional frequency from the Fokker-Planck equation. One of the first who used this approach was H. Dreicer [15]. He assumed collisions of electrons in an infinite, homogeneous, non-relativistic and fully ionized hydrogen plasma with a Maxwellian distribution in an electric field. For larger than thermal velocities, an electron-electron collision predominates, and collisional frequency of electron has a form of

$$\nu(v) = \frac{n_{\mathrm{e}} e^4 \ln \Lambda}{4\pi\epsilon_0^2 k_{\mathrm{B}} m_{\mathrm{e}}^2 v^3}, \tag{3.3}$$

[1] The energy gain of plasma particles is not limited to the electric field. During RF heating of the plasma, the electrons can gain high velocities in the direction of the electric field. Thus, the limited creation of backward runaway electron is possible [14].

where n_e is plasma density and $\ln\Lambda$ is the Coulomb logarithm defined as

$$\ln\lambda = \ln\left(\frac{\lambda_D}{b_0}\right), \tag{3.4}$$

which can be assumed to be constant for tokamak plasma, $\ln\Lambda \approx 15$ [5].

This form of collision frequency holds for hydrogen plasma without impurities with thermal velocities and larger. Therefore, the drag for relativistic velocities is underestimated. Kruskal-Bernstein [16] and Connor-Hastie [17] further developed this solution. As a result, the collisional drag has a global maximum at thermal velocities and a local minimum due to relativistic effects, as shown in figure 3.1. For other than the hydrogen plasma or plasma with impurities, a scaling factor of $(2 + Z_{\text{eff}})$ for collisional frequency (3.3) should be used. The Z_{eff} is an effective ion charge in plasma defined as

$$Z_{\text{eff}} = \sum_i \frac{n_i Z_i}{n_e}, \tag{3.5}$$

where n_i and Z_i is ion species density and charge, respectively. For hydrogen, plasma $Z_{\text{eff}} = 1$. However, plasma impurities raises effective ion charge value.

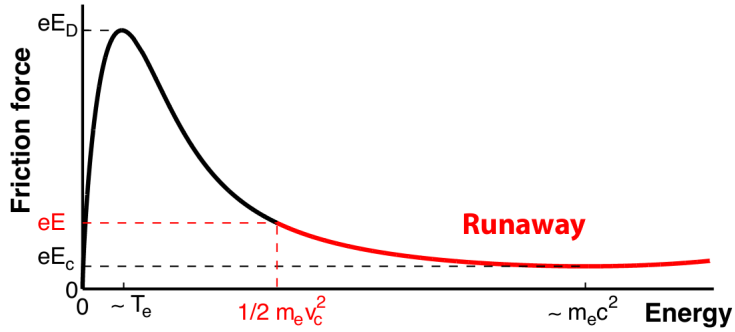

Figure 3.1: Momentum-dependent friction force for a test electron in the plasma in comparison with the driving electric field E. The friction force has a maximum at thermal velocities, v_c presents a threshold for RE emergence [18].

There are two main mechanisms of RE generation. The primary mechanism occurs in an electric field, which is stronger than collisional drag. The secondary mechanism surfaces when an existing seed of runaway electrons multiplies exponentially. Apart from these two, there are other minor ways to push electrons to runaway regions, like tritium decay, cosmic radiation, Compton scattering, magnetic reconnection, and kinetic instabilities [18].

3.1.1 Primary (Dreicer's) mechanism

For electron to become runaway only a strong electric field is needed. From (3.2) and (3.3) at thermal velocity $v_{\text{th}} = \sqrt{\frac{2k_B T}{m_e}}$, a so-called Dreicer electric field intensity can be found:

$$E_D = \frac{n_e e^3 \ln\Lambda}{4\pi\epsilon_0^2 k_B T_e}. \tag{3.6}$$

The Dreicer electric field is a measure of field required for electron velocity increase to exceed the most probable random speed in plasma along with the distance of one mean free path. When this field is exceeded all electrons run away. Fortunately, electric fields in the tokamak plasma do not usually reach this value [19].

On intersection of driving electric field and drag force the critical velocity can be found

$$v_\mathrm{c} = \sqrt{\frac{n_\mathrm{e} e^3 \ln \Lambda}{4\pi\varepsilon^2 m_\mathrm{e} E}}. \tag{3.7}$$

When this velocity is exceeded, the electron runs away. Even though the electric field is not reaching E_D, there are some electrons at the tail of velocity distribution with velocities greater than v_c [2].

A simple estimate of Dreicer runaway production rate can be made with an assumption that all electrons with $v > v_\mathrm{th}$ become runaway within one collision time. This gives a growth rate of

$$\frac{\mathrm{d}}{\mathrm{d}t} n_{\mathrm{RE}_\mathrm{Dreicer}} \sim \frac{eE}{\sqrt{mT}} n \exp\left(-\frac{E_\mathrm{D}}{2E}\right). \tag{3.8}$$

This estimate is too simplistic. The Maxvellian distribution function for supra-thermal electrons can not be assumed. The runaway electrons from the tail of the distribution function are replaced by diffusion, and near v_c, the distribution function becomes directional. This was fixed by Kruskal and Bernstein who divided velocity space into five regions [16]. Then Connor and Hastie used the same approach to derive the runaway growth rate in the relativistic case as

$$\begin{aligned}\frac{\mathrm{d}}{\mathrm{d}t} n_{\mathrm{RE}_\mathrm{Dreicer}} =& Cn \frac{4\pi e^4 \ln \Lambda}{T\sqrt{mT}} \left(\frac{E}{E_\mathrm{D}}\right)^{-h(\alpha, Z_\mathrm{eff})} \times \\ & \exp\left[-\lambda(\alpha)\frac{E_\mathrm{D}}{4E} - \gamma(\alpha, Z_\mathrm{eff})\left(2\frac{E_\mathrm{D}}{E}\right)^{1/2}\right],\end{aligned} \tag{3.9}$$

where

$$\begin{aligned}\alpha &= \frac{E}{E_\mathrm{c}}, \\ h(\alpha, Z_\mathrm{eff}) &= \frac{1}{16(\alpha-1)}\left[\alpha(Z_\mathrm{eff}+1) - Z_\mathrm{eff} + 7 + 2\sqrt{\frac{\alpha}{\alpha-1}}(Z_\mathrm{eff}+1)(\alpha-2)\right], \\ \lambda(\alpha, Z_\mathrm{eff}) &= 8\alpha\left[\alpha - \frac{1}{2} - \sqrt{\alpha^2-\alpha}\right], \\ \gamma(\alpha, Z_\mathrm{eff}) &= \sqrt{\frac{Z_\mathrm{eff}+1}{8(\alpha-1)}}\left[\frac{\pi}{2} - \arcsin\left(1-\frac{2}{\alpha}\right)\right],\end{aligned} \tag{3.10}$$

where C is a constant (in order of unity) of rather mathematical than physical significance.

[2] Note that $v_\mathrm{c} \sim E^{-1/2}$, this hints that non-relativistic assumption does not hold for small electric fields.

This approach also showed that the collisional drag force has a local minimum. This introduces an electric field threshold E_c for RE production in the form of

$$E_c = \frac{n_e e^3 \ln \Lambda}{4\pi\varepsilon^2 m_e c^2}. \tag{3.11}$$

The most of quantities in 3.11 except the density can be assumed constant for tokamak plasma, resulting in $E_c \approx 0.08 \cdot 10^{-20} \cdot n_e$. The experimental data shows that thresholds for observable RE production are $E/E_D \sim 0.02$ and $E \sim 5 \cdot E_c$ [20, 21].

The Dreicer mechanism described above explains the RE generation in small and medium-size tokamaks, since those devices often have favorable conditions for RE generation such as low n_e and high toroidal electric field E_{tor}. The Dreicer's mechanism can serve as the seed of RE, and these electrons are multiplied further by the secondary mechanism.

3.1.2 Hot tail mechanism

During a thermal quench, the plasma electrons slow down and lose energy due to collisional drag. However, the fast electrons have a low collision frequency, and their cooling time is much longer than in the case of thermal electrons. The time between collisions may be comparable to or longer than the time of plasma cooling. Thus, the tail of the hot Maxwellian distribution can stay in the runaway region. Consequently, the number of generated runaway electrons is much larger than predicted by the primary generation rate.

3.1.3 Secondary mechanism

The above-described mechanisms are commonly named primary mechanisms, because they drive thermal electrons into the runaway velocity due to plasma conditions, creating RE seed. However, the thermal electrons can also become REs through knock-on collisions with the already existing REs. While the existing REs stay in the runaway region. Even though the collision frequency of runaway electrons is small, it can be a significant source of RE population growth. This mechanism is called the secondary RE mechanism or avalanche RE mechanism due to the exponential growth of REs. Unlike the Dreicer mechanism, the effect grows linearly with to intensity of the electric field.

Avalanche mechanism can multiply runaway population after thermal quench during Ohmic dissipation of magnetic energy. The runaway avalanche current then overtakes the Ohmic current as the runaway current saturates.

This can be a very intense process in tokamaks with large plasma current, and a small number of initial REs can be multiplied. According to predictions, there is a possibility of transfer of pre-disruption plasma current to RE current reaching up to 10 MA [22].

3.2 Mitigation of REs

During a normal operation of a large tokamak, the REs emerge, but the toroidal electric field is relatively small. Since Dreicer source scales exponentially and avalanche source linearly with electric field strength, the RE growth rate is small. But during disruptions, a number of emerging REs can pose a thread to PFC upon deconfinement. Therefore, the mitigation strategies of RE are tied to disruption mitigation scenarios [18]. Following methods are usually applied when disruptions are unavoidable.

Formation of runaway electrons can be prevented directly by increasing the electron density n_e so large that E_c prevents RE formation through Dreicer and avalanche mechanisms. Because of avalanche mechanism linear scaling with E/E_c, direct prevention of RE involves shatter pellet injection (SPI). For ITER, this scenario will involve up to 32 argon-deuterium pellets injected from three equatorial ports [18].

An indirect approach to RE mitigation is deconfining the REs before their energy can reach too large values. By applying an external periodic magnetic field, magnetic fields can be formed on resonant magnetic surfaces. Magnetic islands are usually unwanted in the plasma because they flatten the profiles of plasma parameters by connecting larger portions of plasma. But chains of magnetic islands can form resonant magnetic perturbations (RMP), increasing RE losses. Even though the RMP runaway suppression was demonstrated in TEXTOR tokamak [23], it is suitable only for small tokamaks since the perturbations decay with increasing distance from the coils. The RMP can not be used on the ITER [18].

3.3 Runaway orbits

REs move along the magnetic field lines as other charged particles in the plasma, but their orbits are generally shifted from magnetic surfaces to LFS because they are opposite to plasma current. Earlier works [21, 24] used a closed circular orbit in a poloidal cross to approximate the RE cross-section of RE movement and showed that the RE orbit shift grows with RE energy. A more detailed approach [25] showed that due to the effects of toroidal acceleration, radiation, and collisions, the orbits are not closed, and RE drifts outward with velocity

$$v_\mathrm{drift} = \frac{qE}{B_\mathrm{t}}. \tag{3.12}$$

For a constant drift velocity, the maximum displacement for one poloidal period can be estimated as

$$d \sim \frac{q\gamma m_\mathrm{e} v_\parallel}{eB_\mathrm{t}}. \tag{3.13}$$

RE electrons from secondary mechanisms can be trapped because they tend to have large pitch angles due to collisions. For those, (3.12) and (3.13) do not apply, since their dynamics is different.

3.4 Radiation loses

The runaway electrons lose energy through radiation caused due to their acceleration following the curved trajectory of the magnetic field line or if they strike the tokamak wall.

3.4.1 Bremsstrahlung

The bremsstrahlung denotes the radiation process which occurs during Coulomb collisions, caused by the abrupt deceleration of the incident particles. The power loss of a single-electron scattered on an ion nucleus is

$$P_{\text{brems}} = \frac{4}{137} n_{\text{e}} (Z_{\text{eff}} + 1) r_{\text{e}}^2 m_{\text{e}} c^3 \beta \gamma (\ln 2\gamma - 1/3), \tag{3.14}$$

where m_{e} and n_{e} are electron mass and density, Z_{eff} effective charge, $r_{\text{e}} = \frac{e^2}{4\pi\varepsilon_0 \text{e} c^2}$ is the classical electron radius and γ and β are Lorentz factor, electron velocity normalised to speed of light respectively [26]. The bremsstrahlung photons are emited mainly in the X-ray spectrum. Bremsstrahlung and interaction of RE hitting the limiter or other PFC is further described in section 4.1

3.4.2 Synchrotron radiation

The RE gyrating around the magnetic field line in a tokamak emits synchrotron radiation. The power loss coming from the synchrotron radiation is approximately

$$P_{\text{synch}} \approx \frac{2 r_{\text{e}} m_{\text{e}} c^3 \beta^4 \gamma^4}{3 R_{\text{c}}^2}, \tag{3.15}$$

where $\mathbf{R}_{\text{c}}$ is the curvature radius of the RE trajectory. It can be calculated from

$$\frac{1}{R_{\text{c}}} = \frac{1-\theta}{R} + \frac{eB\theta}{\gamma m_{\text{e}} c}, \tag{3.16}$$

where $\theta = \frac{v_\perp}{v_\parallel}$ is the RE pitch. [27]. The power of the synchrotron emission depends strongly on RE energy and pitch angle. The pitch angle is affected by the plasma impurity content. The synchrotron radiation tends to increase with the concentration of impurities in plasma [28].

3.5 Diagnostics for RE

RE diagnostic methods rely primarily on the measurements of radiation produced by REs. Diagnostic methods of REs be divided into two groups. The first group focuses on the radiation created by the acceleration of charged particles in plasma. They can measure the properties of the REs confined inside a tokamak. The second group relies on the radiation of the relativistic electrons created upon REs impact into the PFC. In addition, some information can be delivered from magnetic diagnostics if the runaway current is strong enough.

X-rays. X-ray radiation is produced by bremstrahlung. It can be volumetric bremsstrahlung of REs scattered by plasma ions (mostly impurities) or bremsstrahlung produced when REs hit PFC [21].

Synchrotron radiation. The synchrotron radiation refers to light emission by relativistic electrons in a magnetic field. This emission is very strongly forward-beamed, requiring a tangential view.

Electron cyclotron emission (ECE). The ECE in the microwave ($\sim$50–200 GHz) frequency range is one of the earliest tokamak diagnostics. Fast electrons increase ECE signal levels and cause a broadening of the distribution function, but RE ECE is mainly limited to qualitative use [18]

Neutrons. In the presence of sufficiently large RE populations or when using H or He plasmas, neutron production can be primarily due to (γ, n) photo-neutron nuclear reactions in the wall material struck by REs. Photo-neutron signal is typically used as evidence of the loss of high-energy REs from the plasma as the photo-neutron production has significant energy thresholds.

Infrared (IR) thermography. Infrared imaging be used to study the structure of the RE heat loads of the wall. In principle, analysis of IR imaging could deduce the energy flux carried by RE.

Probe diagnostics. Probe diagnostics is limited due to potential damage. The probes can be used limiter shadow (scrape-off layer) to diagnose boundary REs.

Chapter 4

Interaction of ionizing radiation with solid matter

This chapter describes the interactions of ionizing radiation in regard to interactions of high energy electrons.

4.1 Interaction of fast electrons

The primary interactions of energetic electrons with matter are ionization, excitation, breaking radiation (bremsstrahlung), and pair creation. The total energy lost by the particle per unit path length is called the linear stopping power or specific energy loss. It is defined as

$$S = -\frac{\partial E}{\partial x}. \tag{4.1}$$

The specific energy loss through radiation is given as:

$$-\left(\frac{\partial E}{\partial x}\right)_{\mathrm{r}} = \frac{NEZ(Z+1)e^4}{137 m_{\mathrm{e}}^2 c^4}\left(4\ln\frac{2E}{m_{\mathrm{e}}} - \frac{4}{3}\right). \tag{4.2}$$

The factors E and Z^2 show that the Bremsstrahlung is significant only for high electron energies and for absorber material with large atomic numbers.

The collisional loss is defined as

$$\begin{aligned} -\left(\frac{\partial E}{\partial x}\right)_{\mathrm{c}} = \frac{2\pi e^4 NZ}{m_{\mathrm{e}} v^2}\Bigg[&\ln\frac{m_{\mathrm{e}} v^2 E}{2I^2(1-\beta^2)} \\ &- \ln(2)\left(2\sqrt{1-\beta^2-1+\beta^2}\right) + (1-\beta^2) + \frac{1}{8}\left(1-\sqrt{1-\beta^2}\right)\Bigg]. \end{aligned} \tag{4.3}$$

The scattering of electrons is significant immediately after electrons enter the material. Even a material layer with a small thickness can cause significant energy loss and scattering. The electrons lose their energy gradually. In a thick material, electrons can be absorbed and their energy drops to zero.

For materials with a large atomic number, the backscattering process can become significant. The strength of this effect depends on the electron energy

and incidence angle. From molybdenum up to 40 % of electrons can be backscattered. With growing incidence angle θ the number of backscattered electrons scales as $\cosh(B\theta)$, where B is a parameter of material and electron energy [29]. The interaction of high energy electrons (10-600 MeV) with divertor plates in the magnetic field parallel to the material was studied [30]. Due to magnetic configuration, most electrons are deposited in the material within one gyration period length.

4.2 Interaction of X-ray radiation

Almost all REs energy is transferred to photons during the interaction of RE with plasma particles or with the first wall of the tokamak. These energetic photons may interact with matter in different ways depending on their energy and the material. Measurement of X-ray radiation is a fundamental diagnostic for runaway electrons. Photons can interact through photoelectric absorption, Compton scattering, and pair production. Dependence on the incident photon's energy and the interacting atoms of the material is shown in figure 4.1.

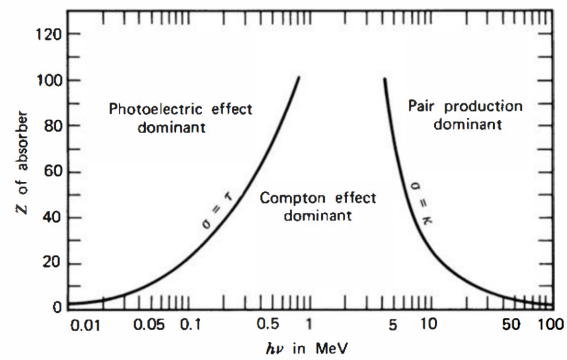

Figure 4.1: Interactions of γ radiation depending on Z of material and photon energy in MeVs. Black curves show values of the Z and energy where the two interactions have the same effect [31].

4.2.1 Photoelectric absorption

In the case of photoelectric absorption, a photon interacts with the atom's electron shell. The incident photon is fully absorbed, and if its energy is larger than the binding energy E_b of the electron, the electron (also called photoelectron) is ejected with energy E given as:

$$E = h\nu - E_\mathrm{b}, \tag{4.4}$$

where h is Planck constant and ν frequency of the photon. After this process, the free electron may interact with other electrons in the material. The electron leaves a vacancy in the shell structure. Then, the vacancy is filled

with an electron from the higher shell. This results in the release of either characteristic radiation or an Auger electron.

4.2.2 Compton scattering

In Compton scattering, an incoming photon of energy $h\nu$ hits an electron at rest. A recoil electron and incident photon are scattered with angle θ (figure 4.2) with respect to the photon's original direction. The energy of the scattered photon is given by

$$h\nu' = \frac{h\nu}{1 + \frac{h\nu}{m_e c^2}(1 - \cos\theta)}, \tag{4.5}$$

where $h\nu$ is energy of the photon prior to the scattering, m_e is the electrons rest-mass.

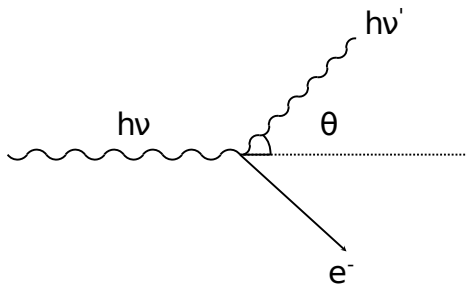

Figure 4.2: A diagram of Compton scattering [31].

The probability of Compton scattering on an atom depends on the number of available targets – electrons and therefore increases linearly with the atomic number Z of the target material [31].

4.2.3 Pair production

When photon energy exceeds double the mass of an electron ($h\nu > 1.022\,\mathrm{MeV}$), pair production may occur. The incoming photon converts into an electron-positron pair within the Coulomb field of a nucleus. The emerging pair carries excess energy. The positron annihilates shortly, producing energetic photons [31].

Chapter 5

Semiconductor detectors

Semiconductor detectors are a type of solid-state detectors used to measure ionizing radiation. The radiation passing through the detector creates a pair of electrons and holes which are separated under an applied electric field. Then the electron and the hole drift to the opposite sides of the sensor, and an induced signal is measured. Properties of a semiconductor material and PN junctions are used to reduce thermal noise. Usually, a number of semiconductor detectors are arranged into the matrix of pixels or sensitive strips.

5.1 Properties of semiconductors

Semiconductors (mostly elements from group IV) crystallize with a surface-centered lattice. A mono-crystal without impurities is called an intrinsic semiconductor. The electrons in a crystal have ranges of allowed energies which form so-called energy bands. These bands are separated by a bandgap, determining the semiconductor material's electronic properties.

An electron with sufficient energy traverses the gap and becomes conductive. The absence of an electron in the valence band will create a vacancy – a hole. This creates two free-charged carriers in the semiconductor material. The energy for creating electron-hole pair in silicon is $E = 3.6\,\mathrm{eV}$. At a non-zero temperature T, spontaneous electron-hole pair formation occurs in the semiconductor with a probability

$$p(T) = AT^{3/2}e^{-\frac{E}{2k_\mathrm{B}T}}, \tag{5.1}$$

where A semiconductor material constant a k_B is the Boltzmann constant.

In addition to the thermal formation, the pair can also be formed by ionizing radiation. However, the resulting pair recombines rapidly unless an external electric field is applied to the semiconductor. In the external field, electrons and holes drift to opposite ends of the semiconductor, to the electrodes. Electron and hole velocities are given by

$$\nu_\mathrm{e} = -\,\mu_\mathrm{e}E, \tag{5.2}$$

$$\nu_\mathrm{h} = \mu_\mathrm{h}E, \tag{5.3}$$

where μ_e and μ_h are mobilities of electrons and holes, respectively, and E is the electric field intensity. The mobility of holes is approximately 3 times lower than the mobility of electrons [31].

The important properties of silicon, the main material for semiconductor detectors manufacturing are in the table 5.1

Property	value	
Lattice constant	5.430	Å
Density	2.328	g/cm^3
El.-hole pair creation energy (300 K)	3.7	eV
Electron mobility (undoped)	1500	$cm^2/(V \cdot s)$
Hole mobility (undoped)	450	$cm^2/(V \cdot s)$
Intrinsic resistivity (300 K)	$230 \cdot 10^3$	$\Omega\,cm$
Breakdown field	30	V/µm

Table 5.1: Important properties of silicon as a semiconductor material [32].

5.2 Extrinsic semiconductors

The deliberate addition of an impurity usually alters the semiconductor material properties. Therefore, depending on the additive, we distinguish semiconductors of two types:

***n*-type.** Semiconductors of type n in which the elements of the V group (of the periodic table), called donors, increase the number of electrons in the conduction band. The donor atom has an extra electron; this electron does not participate in the covalent bond of the crystal. In an n-type semiconductor, there is an excess of electrons; therefore, they are the majority of charge carriers. Minority carriers are holes.

***p*-type.** Semiconductors of the p-type in which the number of valence electrons is reduced by using group III impurities (acceptors). The hole thus formed has a different energy. If this hole is filled with an electron, a covalent bond is created, but one of the atoms is only triple bounded.

The intrinsic (or doped) semiconductor connected to external voltage can not be used as a detector of ionizing radiation. At room temperature thermal creation of pairs results in a current that exceeds the ionization signal by several orders of magnitude. This thermal current can be limited by a p-n junction.

5.3 *p-n* junction

The junction forms the boundary between p- and n-types of the semiconductors inside a monocrystal. The majority of charge carriers of the n-type semiconductor, the electrons, migrate across the junction into the p-type

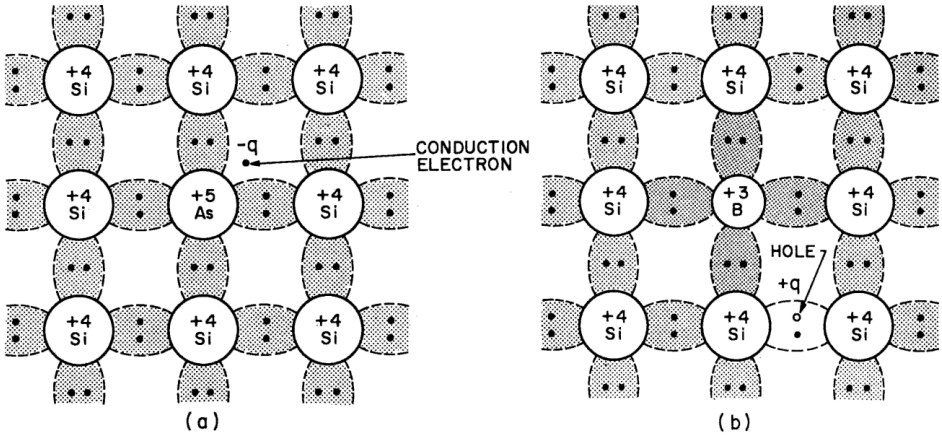

Figure 5.1: Effects of semiconductor dopants:
a) dopants in n-type semiconductors introduce free electrons to semiconductor
b) dopants in p-type leaves holes in crystalline lattice bonds.
Both create new charge carriers [32].

semiconductor. And conversely, the holes move into the n region. This creates a positively charged region in the n semiconductor and a negatively charged region in the p region. The resulting electric field creates a depleted layer where the major charge carriers are not present (figure 5.2).

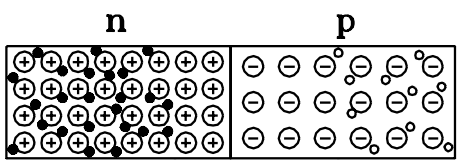

Figure 5.2: The schematics of p-n junction. The area between n and p-type semiconductors in a monocrystal is depleted of free charge carriers and can be used as an ionizing radiation detector [32].

The textitp-n junction constitutes a diode. By applying a voltage in the forward direction, the majority carriers migrate through the junction; therefore, current flows through it. In the reverse arrangement, the majority carriers are drained from the junction. For minor charge carriers, the junction is permeable, but the number of minority charge carriers is inversely proportional to the number of majority carriers.

The electrons and holes that produce ionizing radiation in the depleted region will migrate to opposite parts of the detector and produce a detectable signal. The size of the emptied region is small relative to the size of the sensor, so by applying an external voltage V_b the depleted region is expanded. The thickness of the depleted region d is a function of the voltage applied. It

can be approximated as:

$$d \simeq \sqrt{\frac{2\varepsilon V_\mathrm{b}}{eN}}, \tag{5.4}$$

where ε material permittivity a N dopant content. By increasing the reverse bias external voltage, the depleted area used for detection can be expanded.

Charge-sensitive amplifiers are used to amplify the signal from the detector, so it is desirable to keep the capacitance of the textitp-n junction as small as possible. From the thickness of the depleted region, we can derive a relationship between the capacitance

$$C = \frac{\varepsilon S}{d} \simeq S\sqrt{\frac{e\varepsilon N}{2V_\mathrm{b}}}, \tag{5.5}$$

where S the is junction cross section. As the voltage V_b increases, the junction capacitance decreases and the detection properties of the semiconductor improve. However, the external voltage cannot be increased arbitrarily, as it may break the junction [31].

5.4 The strip detector with PH32 ASIC

The PH32 ionizing radiation detector (figure 5.3) consists of a segmented semiconductor sensor with 32 strips. PH32v8 Application Specific Integrated Circuit (ASIC) processes measurements [33].

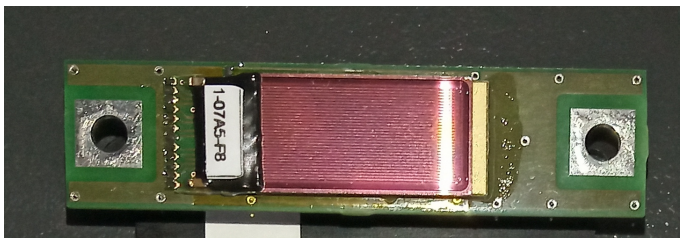

Figure 5.3: The 32-strip silicon detector is connected to PH32v8 readout chip.

5.4.1 Sensor

The sensor consists of 32 strips, each with dimensions 250 µm × 18 mm. Strips are of n^+-on-p type silicon, a high-resistivity substrate with 525 µm thickness. The capacitance of each strip is ≈ 4.6 pF. The full depletion of the sensor occurs at −150 V bias voltage [34]. The schematic cross-section of the sensor with all semiconductor and metal layers is shown in figure 5.4

5.4.2 PH32 readout chip

The PH32v8 is a front-end chip for the detection of ionizing radiation. It was developed at the Centre of Applied Physics and Advanced Detection Systems

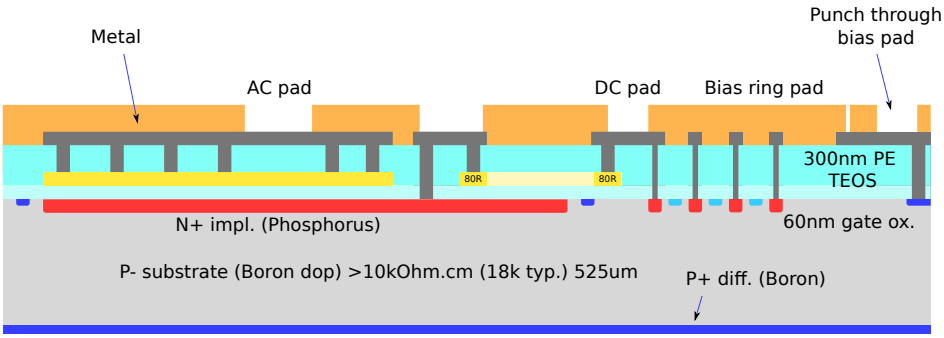

Figure 5.4: The schematic cross-section of the sensor, showing the different materials and layers that comprise the sensor.

in CTU. The PH32 chip with dimensions of 3.5×2 mm^2 is manufactured using 180 nm CMOS technology. It can measure the charges generated in the sensor, count number of hits, and measure the time of particle arrival. The chip has 32 input channels. The analog block processes each channel input, and then information on the number of hits, measured charge, or time of arrival is stored and processed in the digital block. The digital block is also responsible for communication with Simple USB Readout Equipment (SURE), through which it is possible to communicate with a computer [34].

Analog block

The signal from a sensor is transferred through a coupling capacitor, and then it is amplified by Charge-Sensitive Amplifier) (CSA). This amplified signal is compared with the threshold value by a discriminator. The digital block of a channel then processes the discriminator's resulting signal. The CSA can operate in two modes of sensitivity. The low gain (LG) mode is suitable for small charges generated by the sensor, i.e., detecting charged ions and alpha particles. The high gain (HG) mode is suited for detecting low-energy X-rays and β-radiation. Each channel has multiple digital to analog converters (DAC) designed for tuning the channel output. DACs operate in pairs, one for chip-wide settings, shared between channels, and other more finely tuneable DACs for per-channel adjustments. Tuneable parameters are CSA feedback current and discriminator threshold. By adjusting these DACs, it is possible to ensure equal output for the same charge in different channels [34].

Digital block

The digital part is responsible for managing the configuration of DACs, processing input from discriminator output of analog block, and communication with SURE.

The signal from the discriminator is processed in the digital part of the chip. Input is processed when the digital shutter is open. Channel can be

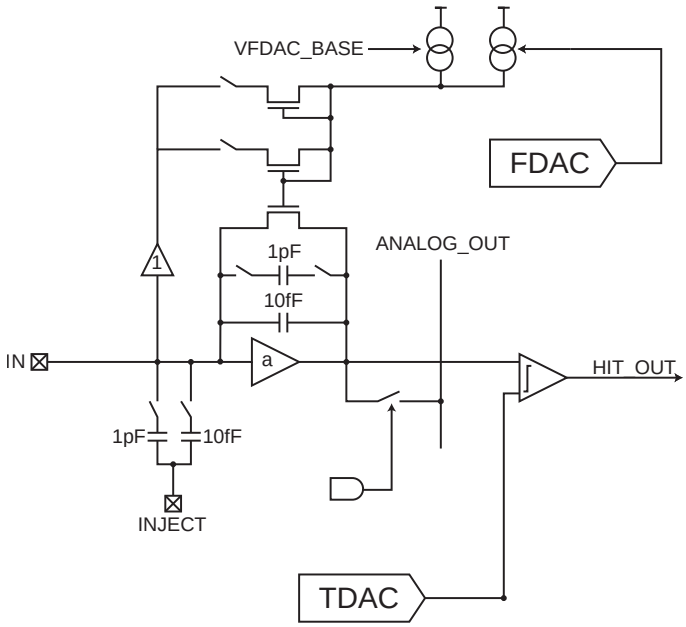

Figure 5.5: Diagram of the analog part of the ASIC detector PH32. Converters TDAC and FDAC are used for tuning the discriminator output. Signal passes from left (IN) to right (HIT OUT). At first the signal is amplified by CSA. CSA is tuneable by FDAC. The is the signal compared with threshold to limit intrumental noise. Threshold can be set by TDAC [34].

configured to four different modes of signal processing:

- **Hit count** – counts how many times the threshold has been exceeded during the acquisition time.
- **Deposited energy** – using the internal clock, time over the threshold is measured. The height and duration of the pulse are proportional to deposited ionization energy.
- **Energy of the first hit** – similarly to the previous mode, the energy of the first detected particle is measured.
- **Time of arrival** – the time between particle detection and the end of the shutter measured. This can be used to compute the time of flight of the detected particle [35].

The output from the sensor, discriminator, and illustration of modes function is shown in figure 5.6. Measurements are stored in 16 bit asynchronous counter with overflow control. After acquisitions, data can be read by SURE interface. Time for readout and reset of the counter yields the detectors' dead time. It is approximately 75 µs.

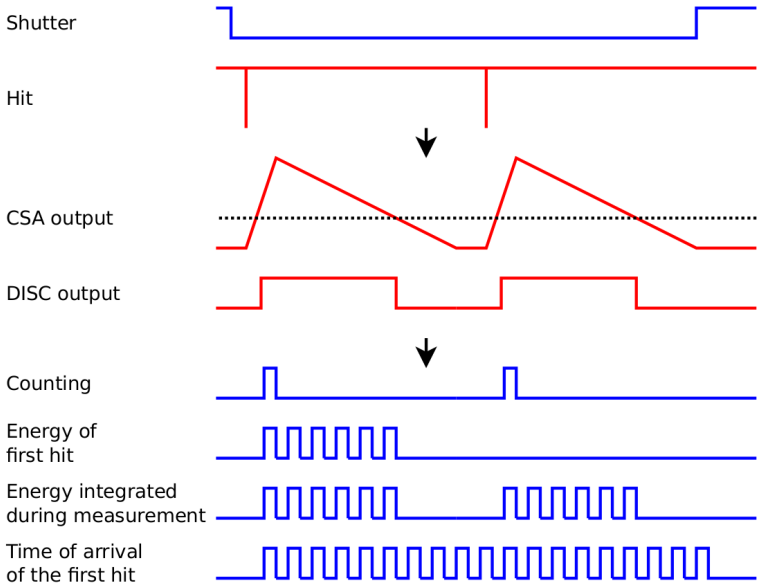

Figure 5.6: Principle of signal processing in a PH32 chip: Digital part signals are in blue, and analog block signals are red.
From the top: open/closed shutter, particle hit on the sensor, output of CSA, discriminator output.
Based on chip settings: hit counting mode, ToT of the first hit, total ToT time of arrival measurement In hit counting mode a one clock cycle is added to register on hit. In energy measurement the for tome over threshold the clock count is added to the register. Time of arrival mode accumulates clock tics to the end of the shutter [33].

Chapter 6

Scintillation detectors

Scintillation detectors are widely used in nuclear, particle and medical physics. This type of ionizing radiation detector comprises of scintillator and photodetector. A scintillator is a material that emits light when it is excited by ionizing radiation. The photomultiplier, either PMT or photodiode is used for conversion and amplification of light pulse into an electric signal.

6.1 Scintillators

Many materials exhibit scintillation properties, but most commonly used are inorganic crystals or organic materials.

The characteristic parameters of the scintillator are its density, scintillation efficiency, light yield, emission spectrum, and decay time of the scintillation light. The scintillation efficiency $\varepsilon_{\mathrm{sc}}$ is defined as the ratio of the energy of the emitted photons to the total energy absorbed in the scintillator material. The light yield γ is the number of photons per 1 MeV of energy absorbed in the scintillator. From the emission spectrum, the maximum at a characteristic wavelength λ_{max} should couple with the photodetector. The scintillation light pulse has a rapid rise in intensity followed by a much longer exponential decay with a decay time τ_{D} characteristic of the scintillation material. Organic and inorganic scintillators differ in principle responsible for light emission and have different characteristics. Properties of selected scintillation materials are in table 6.1.

material	light yield [photons/MeV]	τ [ns]	λ_{max} [nm]	n [-]	ρ [g·cm^{-3}]
NaI(Tl)	38000	230	415	1.85	3.67
LSO	25000	47	420	1.82	7.4
LYSO	27600	45	420	1.81	7.1
YAP	18000	27	370	1.95	5.37
$LaBr_3$:Ce	63000	20	380	1.9	5.08
$CeBr_3$:Ce	60000	19	380	2.09	5.1

Table 6.1: Properties of selected scintillation materials τ – decay time, λ_{max} wavelength of maximum emission, n – reflective index, ρ – density [31, 36, 37, 38]

In comparison to semiconductor detectors much larger energy is required for the generation of one photoelectron than it is necessary for the creation of one electron-hole pair in solid-state detectors. Energy about 50 eV is necessary for the best scintillation counters to produce the light signal.

6.1.1 Inorganic scintillators

Inorganic scintillators are typically crystals. In comparison to organic scintillators, they have a higher light yield but a longer decay time. In addition, since inorganic scintillators have a high atomic number and density, they are better suited for γ ray spectroscopy.

6.1.2 Organic scintillators

Organic scintillators are made of aromatic hydrocarbon in benzene ring structures. They are mainly plastics, liquids, or rarely crystals. Organic scintillators have a shorter decay time but smaller light yield, which is non-linear for larger energies deposited.

6.2 Photodetectors

6.2.1 Photomultiplier tube

PMT is an evacuated glass tube containing a photocathode, a series of dynodes, and collecting an anode, as shown in figure 6.1. The photocathode converts incident light photons into low-energy electrons via the photoelectric effect. The produced photoelectrons are focused by an electric field at the first dynode. At the dynode, the number of electron is multiplied with a process similar to the photoelectric effect. The first dynode is held at potential around 300 V and each following dynode is typically 50-100 V greater than the previous one. Each dynode further multiplies the number of electrons, thus the gains up to 10^7 are possible. The PMT is sensitive to magnetic field, which can defocus electron beam between dynodes causing the reduction of the gain [31].

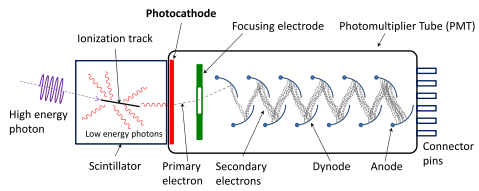

Figure 6.1: A schematic of a scintillator detector consisting of scintillation crystal and photomultiplier. A high-energy photon is converted to visible light in the scintillator. A visible photon is converted to an electron via the photoelectric effect and consequently amplified by series dynodes in a photomultiplier [39].

6.2.2 Silicon photomultiplier

A silicon photomultiplier (SiPM) is a solid-state, light sensing device capable of detecting single photons. The SiPM consists of multiple avalanche diodes. These diodes are designed to work with large reverse bias thus on interaction with photon a drifting electron have enough energy to create additional pairs in avalanche and a so-called Geiger-mode discharge occurs. The current in the diode is quickly stopped by a passive quench resistor. A pair of the diode and quenching resistor acts as a single photon trigger. Multiple optically isolated photodiodes are integrated into one output forming a microcell. Each microcell detects photons individually. The output is summed through the whole SiPM. The result of the readout is an analog signal with an amplitude proportional to the magnitude of photon flux.

The absorption length of a photon in silicon depends on its wavelength. The mean photon absorption length in silicon is on the order of 0.1 µm at a wavelength of 400 nm and increases to about 10 µm at 800 nm. This characteristic makes silicon a good photodetector material in the spectral range of 400 nm to 800 nm which corresponds well with the 420 nm optical photon emission peak of LYSO.

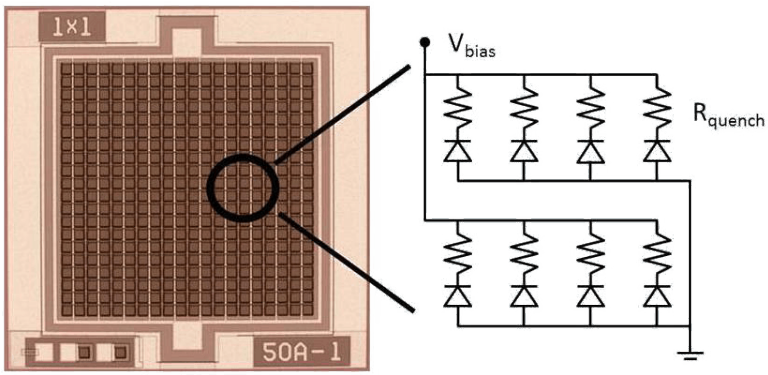

Figure 6.2: Silicon photomultiplier and connection schematics of one microcell coposed of diodes and quenching resistors [40].

A bias voltage for creating a depletion region in SiPM is called as the breakdown potential, V_{br}. It is usually in order of 20-70 volts. SiPM is typically operated a few volts above this breakdown potential. This additional potential, the over-voltage, ΔV varies from device to device. It is typically around 2-5 volts. The operating potential of a system is defined as

$$V_{\mathrm{bias}} = V_{\mathrm{br}} + \Delta V. \tag{6.1}$$

Gain

Applied bias voltage strongly affects the gain, because the bias voltage increases the electric field strength across the avalanche layer. The ratio of the total microcell output charge to an electron charge e gives the SiPMs

gain or ionization rate. The total charge is calculated by multiplying the microcell capacitance C by overvoltage ΔV as

$$G = C\frac{\Delta V}{e}. \tag{6.2}$$

Noise

SiPMs have a specific signal noises, some of which is not present in vacuum PMTs. They include dark count, optical crosstalk, and afterpulses.

Dark count. Thermal electrons can trigger an avalanche in SPAD, this creates a single-photon signal in SiPM. The dark count is measured in pulse rate or pulse rate per area. The amount of noise-pulses increases with temperature and bias voltage. These pulses are called dark count pulses because they are problematic in low photon fluency measurements.

Optical crosstalk. During the breakdown in the diode, photons can be emitted. These photons can affect the neighboring cell either directly or they can be reflected from the collecting window back to the SiPM. This can trigger the neighboring cell causing the optical cross talk. An emitted photon may be absorbed by the same pixel, so the possibility of crosstalk decreases with microcell size.

Afterpulses. When microcell voltage is quenched to stop the Geiger discharge, some photoelectrons may be trapped by the lattice defects. After recovery to a bias voltage, this can trigger a new pulse following the true signal. Afterpulse depends on the bias voltage, doping level design of SiPM, recovery time, and temperature. At high temperatures, the trap carries lifetimes are shorter, so the afterpulsing effect becomes weak at the fixed repetition time. The probability of trapping carries inside the crystal increases with lower temperature due to become long carries lifetime, therefore after pulse ing effect will increase

Chapter 7

Monte Carlo particle transport simulations

The Monte Carlo method is a numerical technique relying on random number generation to calculate probabilities and corresponding quantities, which are too complex to solve analytically. It is often used to solve high-dimensional optimization problems, calculate multidimensional integrals, or sample numbers that follow a particular probability density function. Monte Carlo methods can accurately model the physical processes which occur during the particle transport in media. However, because of its stochastic nature, simulation of a large number of particle histories is required to achieve the desired statistical accuracy. Some of the most general-purpose MC-based simulation codes for radiation transport include MCNP, Geant4, Fluka, and PENELOPE. The simulations perfomed within the scope of this thesis were done using GEometry ANd Tracking (Geant4) toolkit.

7.1 Geant4

Geant4 is an open-source C++ toolkit developed explicitly for simulations of the interaction of ionizing radiation with matter [41]. It is developed by a worldwide collaboration of high energy physicist, mainly simulate detector arrays in CERN. It covers a wide range of hadronic, electromagnetic, and optical processes over an energy range from a few eV to up to several TeV.

Geant4 applications have a highly modular structure. The physics processes and models are implemented in these applications by exploiting the object-oriented nature of its programming language.

Although the modular structure of Geant4 puts only very few limits, a user must implement a few mandatory classes for the simulation to work. These mandatory user classes comprise the detector construction, primary particle generation, and the physics list.

Geant4 simulation initiates primary particles and iterates through particle trajectory. The surrounding material and it chooses the next steps based on physics processes included in the physics list. Based on these processes, the parent particle may undergo any number of processes. During detector construction, a volume can be declared to be sensitive, then interacting particle properties can be recorded.

7.1.1 Physics list

Geant4 provides preconfigured physics models optimized for various general fields of physics covering the energy range from eV to TeV. For modeling of RE response to strip detector, a `FTFP_BERT` physics list implementation was used. Part of this list is `G4EmStandardPhysics` which describes all processes in chapter 4.

7.1.2 Geometry

The main concepts of Geant4 geometries are physical and logical volumes. A logical volume can contain other volumes and it has associated with it all the specifics and information not having anything to do with physical placement such as materials and electromagnetic fields. A physical volume is the physical location and orientation of a detector element. All physical volumes must be placed in one world logical volume.

Objects in Geant4 simulation can be either implemented manually in C++ code or imported from Geometry Description Markup Language) (GDML). For faster prototyping and interchangeability of different geometries `pyg4ometry` python package was used to model and convert CAD formats into GDML [42]. Scripts for generating geometries in `pyg4ometry` are similar to C++ Geant4 code, but trough scripting it is possible to make multiple variansts of each geometry quickly without need to recompile C++ code.

7.1.3 Magnetic Field

A `FieldManager` class can be attached to any logical volume and provides a description of an electromagnetic field. User can choose from predefined fields like uniform or quadrupole fields. Or it is possible to define arbitrary fields varying with both space and time.

For particle movement in a magnetic field, an integrator must be selected. Geant4 provides multiple RK steppers and 'Helix' steppers which assume slowly varying pure magnetic fields. They are optimized for helical particle motion.

Because particles in magnetic fields can loop in magnetic volume without interacting with another volume, a user-defined maximum length of particle tracks in the magnetic field can be set.

7.2 Strip detector model

GDML model of PH32 detector is shown in figure 7.1. The detector consists of two PCBs made of FR4 (glass-reinforced epoxy laminate) material in the figure 7.1 shown in green. Behind the epoxy resin (in black) is the PH32v8 chip (blue). The sensor is composed of 32 strips. Both strips and chip are described as made from silicone and set to be a sensitive volume. This enabled the acquisition of deposited energy, and the number of interactions from each strip and evaluation of the PH32 chip is sufficiently shielded.

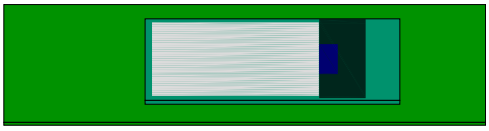

Figure 7.1: The visualization of a GDML model of PH32 strip detector.

Material	Formula		Source
Vacuum	-	$1 \cdot 10^{-12}$	GEANT4 NIST Material Database
Silicon	Si	2.33	GEANT4 NIST Material Database
Glass	SiO_2	2.32	GEANT4 NIST Material Database
Epoxy	$C_1O_1H_1$	1.0	[43]
FR4 (circuit board)	$\frac{SiO_2}{Epoxy} = \frac{52.8}{47.2}$	1.86	[44]

Table 7.1: Materials used in GDML model of PH32 detector.

The materials used in the strip detector model are in table .

7.2.1 Strip detector setups

To test different setups of PH32 detectors and their shielding multiple detector geometries were created. These setups consist of one or two instances of strip detectors described in the previous section.

Simplified two detector vertical setup

This setup consists of two PH32 detectors placed vertically in a vacuum vessel, each facing an opposite direction (figure 7.2(a)).

Two detector vertical setup

Modification of the vertical setup with both detectors rotated by 45°. Therefore the edge of the sensors is closer to the plasma edge (figure 7.4). Also, it increases resolution in the radial direction at the expense of effective detector depth.

Two detector vertical setup with a metal case

After realising the detector was physically constructed, the previous model was updated. To reflect the actual model with an aluminum case.

7.3 World models

To simulate the detector in different conditions two world volumes in which the detector can be placed were constructed. The first is a simplified linear model with a magnetic field and limiter. The second, is toroidal to represent the conditions in GOLEM tokamak more accurately.

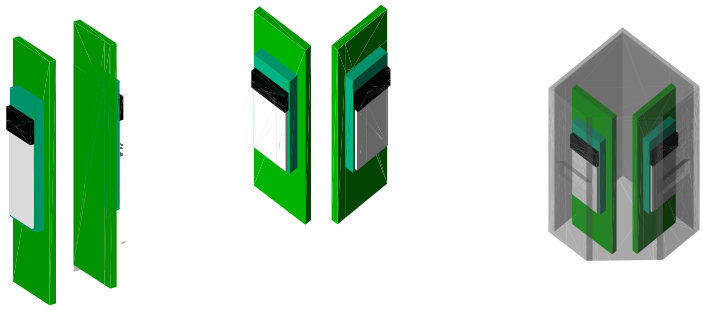

(a) The GDML model of vertical setup

(b) The GDML model of simple vertical setup

(c) The GDML model of vertical setup in a metal case

Figure 7.2: Visualisation of GDML models of different PH32 setups. PCBs in green, sensor in white, epoxy resin cover of PH32 chip in black and aluminum case in grey.

7.3.1 Linear model

From previous work [45], it was suggested that RE backscattering may play a role in diagnostics of RE in GOLEM tokamak limiter shadow. To investigate this effect a linear version of the vacuum vessel was constructed. The linear model GDML model is shown in figure 7.3. The model consists of a tube (light grey) – a vacuum vessel, and a limiter (brown). The RE source is placed on the left to simulate the scrapping of RE against the limiter. To investigate the role of backscattering, a 'second' limiter can be placed to the opposite of the tube. Then the detector placed in the middle interacts with the RE beam and optionally with the backscattered electrons. Because the movement of REs is governed by magnetic filed, the simulation volume can be magnetized with axial field of strength described by (2.1) and angular field described by (2.5) so the effect of field helicity can be studied.

7.3.2 Simplified tokamak model

This model should represent the situation on GOLEM tokamak more accurately. The model consists of a toroidal vacuum vessel (liner) with one port cross (shown in grey) and a poloidal limiter (in brown). The dimension and material of the vacuum vessel and limiter follow the real version of GOLEM tokamak. The volume inside the vacuum vessel is magnetic. The magnetic field is modeled by equations (2.1) and (2.7).

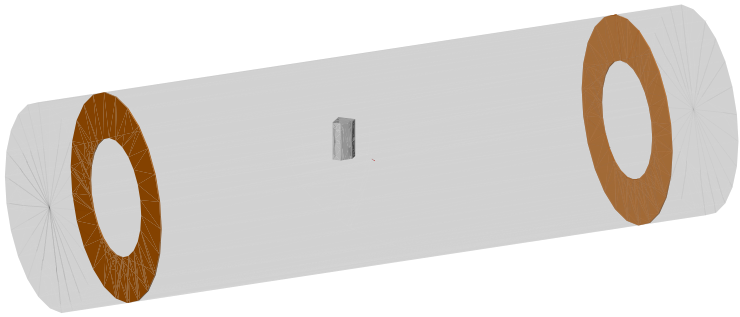

Figure 7.3: The visualization of a GDML linear model for backscattering studies. Grey magnetic vacuum volume, one molybdenum limiter brown, second limiter in light brown is optional in this model. The REs are generated on the left side. They trough fisrt limiter, on its edge some scattering of REs may occur. They RE pass trough volume with the detector and if is second limiter present they can backscatter back towards the detector. The vertical setup of strip detector for reference.

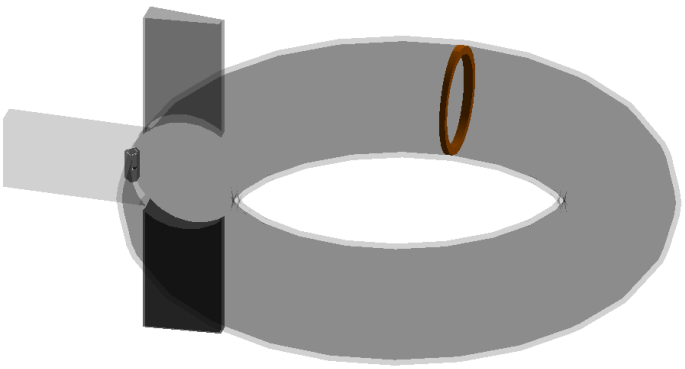

Figure 7.4: Simplified GDML model of the tokamak.

Chapter 8

Results

8.1 Geant4 simulations

8.1.1 Backscattering in a magnetic field

A simulation with a linear model was performed to estimate the number and energy of backscattered REs from the limiter. The simulation was performed with a uniform magnetic field of 0.2 T and with different RE energies and pitch angles.

Figures 8.1(a)-8.1(c) show the energy distribution of the backscattered the REs. For larger pitch angles, the energy of backscattered REs tends to be larger but the total number of the backscattered electrons does not change significantly with their energy, as shown on figure 8.1(d). For small pitch angles, the portion of backscattered REs is in accordance to [29]. With larger pitch angles the portion of the backscattered electron increases. The backscattered REs follow the magnetic field line back to the source. Their spread in the direction perpendicular to the magnetic field line is governed by their Larmor radius.

Effect of poloidal magnetic field

Magnetic field lines are curved inside a tokamak. Thus, the RE strikes limiter under the angle determined by edge safety factor q_{edge} and theri pitch. For typical safety factor on GOLEM tokamak's plasma edge $q \sim 6$ the incidence angle will be changed by 3° which does not affect the backscattering much.

Effect of tokamak geometry

A test run of simulation with simplified tokamak model was done. It showed that backsattering is still present in this model, but because of toroidal nature of the model, some particles become trapped in magnetic field without interacting with either tokamak wall or limiter. Even though Geant4 removes these particels from simulation if they reach certain distance, but they extended the time needed for simulation to finish. A number of particles drifted towards vacuum vessel, there their energy was deposited (as is predicted by [30]).

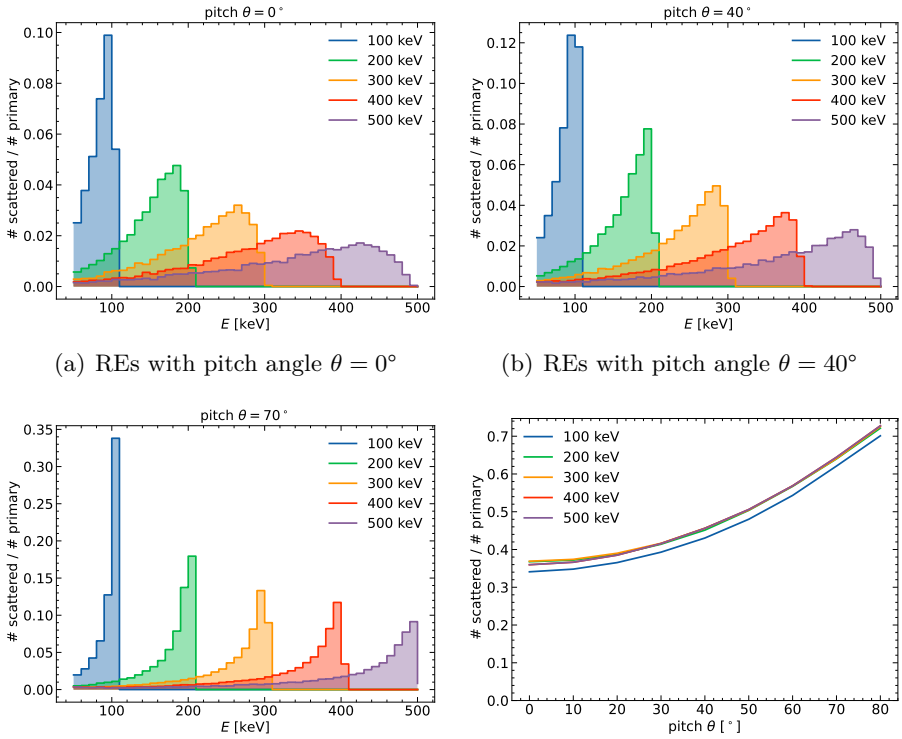

(a) REs with pitch angle $\theta = 0°$

(b) REs with pitch angle $\theta = 40°$

(c) REs with pitch angle $\theta = 80\,°$

(d) A number of backscattered REs as a function of pitch angle.

Figure 8.1: Results of Geant4 simulation of REs backscatering on molybden limiter in 0.2 T field perpendicular to material surface. Simulation was performed for pitch angles in range from 0° to 80°, with 10° step. Primary RE energies were seeded with energies 100, 200, 300, 400 and 500 keV

8.1.2 Strip detector response to REs

Figures 8.2(a) and 8.2(b) show detector response to a 500 keV RE beam in a linear model both with magnetic field and without and with RE backscattering, respectively. The simulation was repeated for different six distances of detector from the limiter edge. In the upper part of the figure is the response of the detector oriented opposite to plasma current, i.e in the direction of incoming REs. On the lower part, it the response from the detector oriented in direction of the plasma current i.e. facing away from the RE beam is shown.

The edge of RE is clear for the detector facing the beam. Due to the scattering of electrons with detector and detector cover, the edge of the detected beam, some electrons are also registered by detector facing in the opposite direction, as shows the sharp edges on lower parts of figures. The scattering of REs causes 'cross-talk' between detectors. The REs backscattered from the limiter produce a spatially uniform signal in the second detector.

HXR spectrum reproduced by LYSO scintillator measurements in section 8.2.2 suggests that RE energy may be larger than was expected. Therefore, additional simulations with larger RE energies were performed. The results

of simulation with 1 MeV REs are in figure and with 1.5 MeV REs in figures 8.2(c)-8.2(f). Due to scattering, the edge from RE detection is fuzzier. The not-backscattered REs affect more the detector oriented in opposite direction.

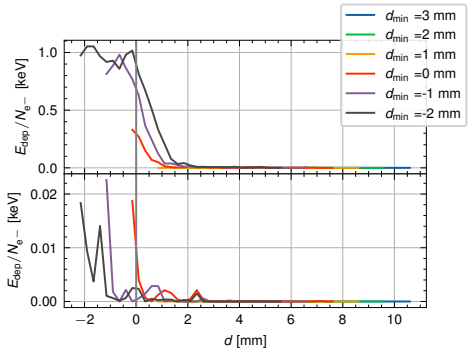

(a) 500 keV REs, no backscattering.

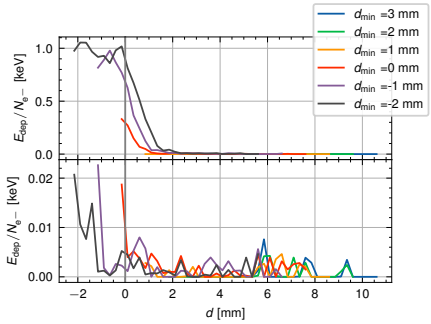

(b) 500 keV REs, with backscattering.

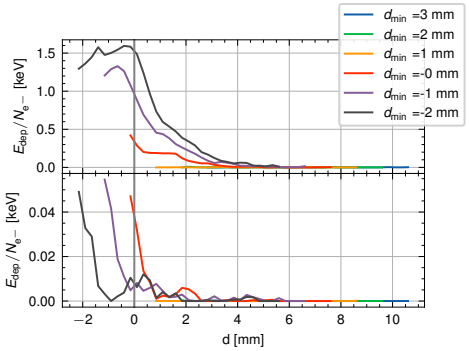

(c) 1000 keV REs, no backscattering.

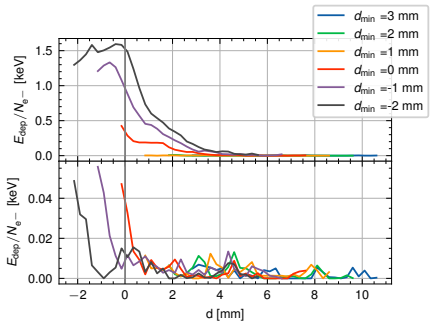

(d) 1000 keV REs, with backscattering.

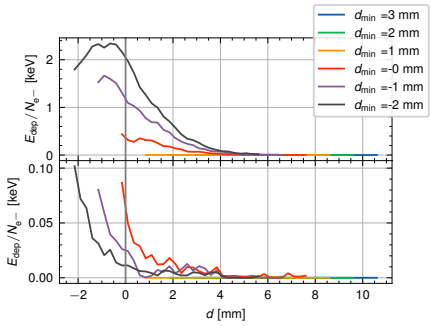

(e) 1500 keV REs, no backscattering.

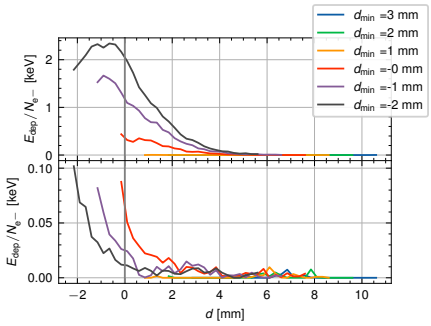

(f) 1500 keV electrons, with backscattering.

Figure 8.2: Result of Gean4 simulation of strip detector response to REs. The electrons were seeded in front of the 'first' limiter. The scrapped electron interacted detector and in case of 8.2(b), 8.2(d) and 8.2(f) REs were backscattered by the 'second' limiter. The detector oriented towards RE source plotted in upper plot. On the lower plot, the detector oriented toward limiter is shown. Deposited energy normalized to 50 000 generated primary electrons are shown as a function of distance from limiters edge d_{lim}. The simulation was repeated for six different distances from the limiter.

8.2 Experiments on GOLEM tokamak

8.2.1 Setup

The setup prepared for experiments follows the vertical model described in 7.2.1. Two strip detectors were placed in aluminum encasing to provide shielding from magnetic fields and HXR holes were covered with thin aluminum foil (figure 8.4). The detector was placed in the NE vertical port of GOLEM tokamak 90° in the toroidal direction from the limiter as shown in the figure 8.3. The tokamak discharge is a source of wideband electromagnetic pulse. To limit the noise, the bias of −100 V and power for the detector was provided by batteries, and data were collected via optical USB cable to ensure galvanic separation from the vacuum vessel and power grid.

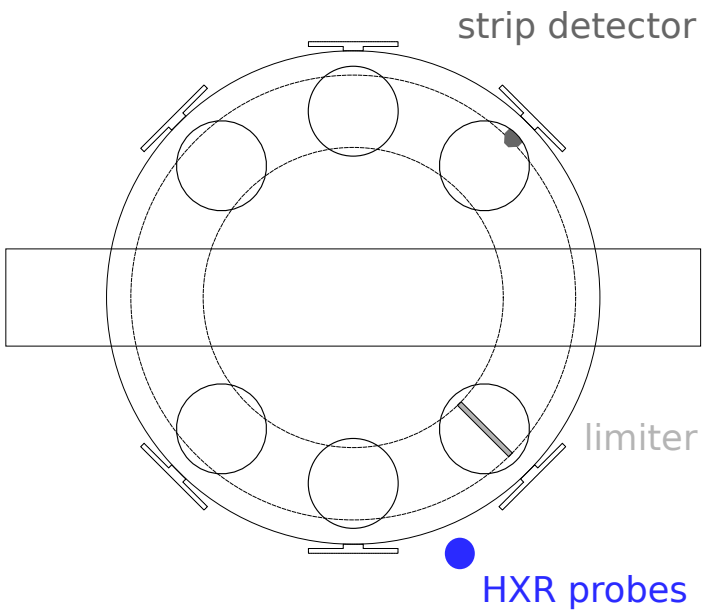

Figure 8.3: The schematic top view for GOLEM tokamak with marked strip detector and scintillator detectors positions.

RE at GOLEM tokamak

Using the q estimate for GOLEM plasmas (2.8), drift velocity at plasma edge can be written as:

$$v_{\mathrm{drift}} \sim \frac{U_{\mathrm{loop}} a^2}{\mu_0 I_{\mathrm{p}} R^2}. \tag{8.1}$$

From shots presented in this section only a portion of them has reliable measeurements of U_{loop} and I_{p} since data acquisition system are not tuned for discharges in anticlockwise direction. The values of U_{loop}, I_{p} and v_{drift} are

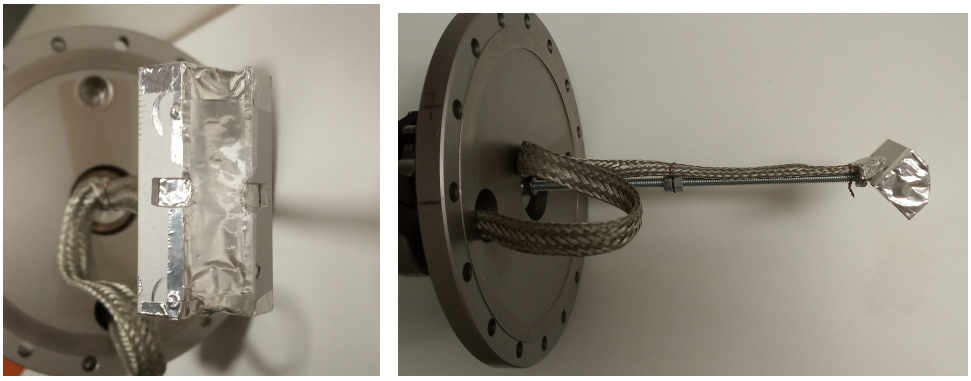

Figure 8.4: Photos of setup with two strip detectors mounted on the manipulator.

shown in figure 8.5. RE drift (8.1) scales with plasma resistivity at GOLEM tokamak. This value can not be easily scanned.

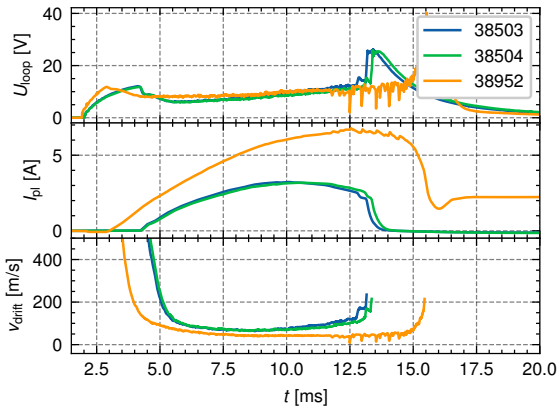

Figure 8.5: Values of loop voltage U_{loop}, plasma current I_{p} and estimated RE drift velocity $v_{\mathrm{drift}}(a)$ at the plasma edge. Selected shots. The RE drift velocity is large at plasma breakdown, during discharge this value is stable.

From (3.13) the energy limit for runaway orbit for GOLEM tokamak plasma with parameters $B_{\mathrm{t}} \sim 0.8\,\mathrm{T}$ and $q \sim 2$ is estimated to be 5 MeV. For typical parameters mid-discharge $B_{\mathrm{t}} \sim 0.2\,\mathrm{T}$ and $q \sim 6$ RE energy limit is $\sim$1 MeV.

There are some studie of RE energy on GOLEM tokamak: the [11] suggests that RE energy on GOLEM tokamak have energies around hundered of keV. A study by [46] indicates that on the beginning of discharges RE energies are around 300 keV. Due to pile-up in HXR singnals the energy estimates for whole discharges was not possible. The [47] measurements shows that REs energy at GOLEM tokamak is around 600 keV.

8.2.2 HXR spectractrum reconstruction

The data from HXR probes are shown in the figure 8.6(a), in 8.6(b) in more detail. All pulses from HXR photons are piled up, but still, the pulses from

LYSO coupled with SiPM can be clearly identified. This allows to identify pulses' location temporal during plasma discharge, then they can be fitted with pulse function. As a result, the height of superimposed pulses and therefore the spectra of the HXR signal can be reconstructed. The figure 8.6(c) shows a comparison between the original and reconstructed HXR signal and shows 8.6(d) original spectra from pile-up and reconstructed spectra.

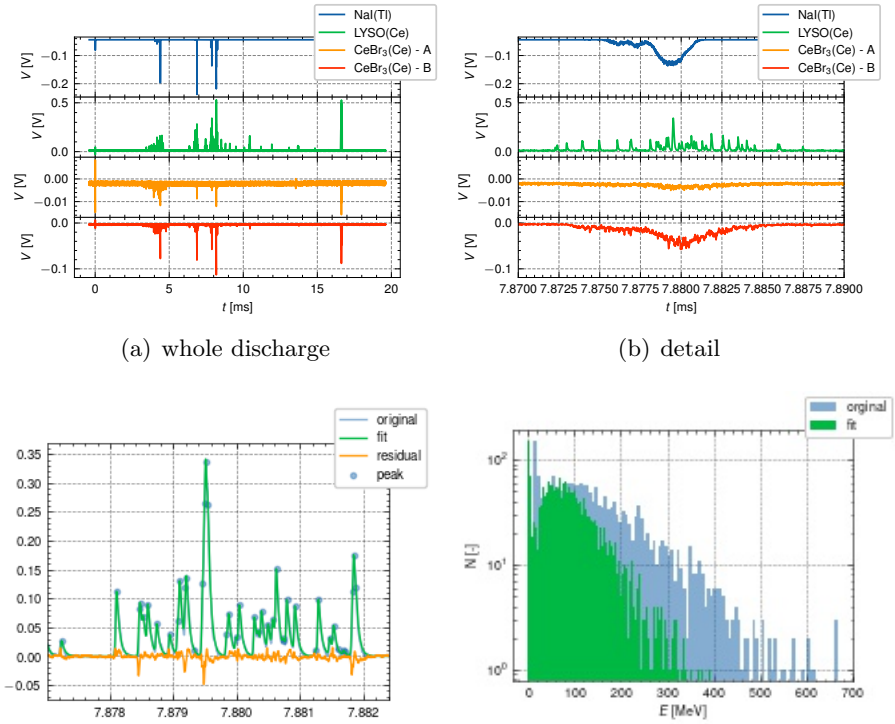

(a) whole discharge

(b) detail

(c) the fit of LYSO waveform

(d) Energy spectra original and corrected for pile-up

Figure 8.6: #37150 waveforms recorded from HXR probes present at GOLEM tokamak

8.2.3 Strip detector

In this section data measured with strip detectors are presented. Most figures consist of two plots. The upper plot always shows the strip detector oriented in opposite direction to the plasma current. This plot should represent energy deposited to the detector by incoming REs. The lower part shows the measurements from detector oriented towards plasma current. Energy deposited to this detector should be mainly from backscattered electrons.

From Geant4 simulation, it is expected that the response of the detector would look like figure 8.7.

Discharges are not presented in the order they were conducted but by the distance of the detector from the plasma edge.

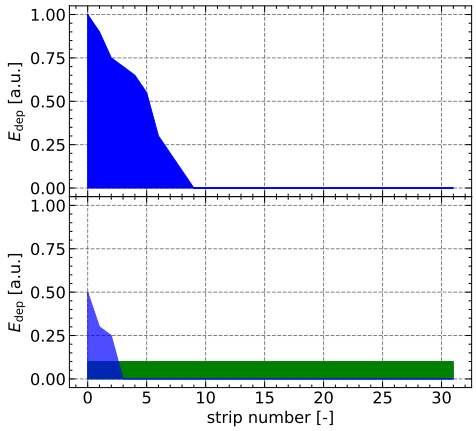

Figure 8.7: Response of strip detector to REs as is expected from simulations. In blue, signal from normal REs, in green signal from backscattering of REs on limiter.

Shot #38514

Figures 8.8 shows results from discharge #38514, performed with plasma current and toroidal magnetic field in the anticlockwise direction. In figure 8.8(a) it can be seen that strip detector becomes saturated at the beginning of the discharge, even if the number and energy registered by the LYSO scintillator are low. After 14 ms no particles are registered by strip detector. This can be caused by a shift of plasma position, as plasma on GOLEM tokamak tends to shift upward. Unfortunately, there are no measurements available of plasma position in this discharge.

Profiles of measured energy deposition from the start of the discharge are shown in figure 8.8(b). The response from the detector collecting incoming REs has the expected shape, while the detector oriented in collecting particles in direction of plasma current is saturated. At the time interval between 12 and 13 ms the greater energies are registered at a larger distance from the limiter. This could be probably attributed to RE drift described by (8.1), but further investigation is needed.

Shot #38289

Figures 8.9 show RE energy measurements from two strip detectors using the ToT method. Six measurements between 2 and 3.2 ms is shown in figure 8.9(b) as function of strip number i.e the distance from limiter edge. During this discharge, the detector was placed in limiter shadow at distance $d = 8$ mm from the limiter's edge.

The first detector registered incoming REs only on the edge of the sensor closer to plasma. For strips 0-17, the response of the second detector is the same as the first one. This could be an effect of electrons scattering on the detector and the detector cover. This seems to be in accordance with the results of the simulations, but the effect is more prominent. On strips

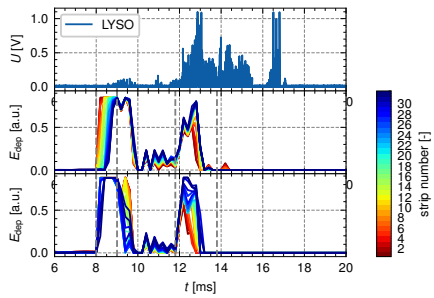

(a) Data from the whole discharge. LYSO scintillator and two strip detectors Every line represents one strip color – coded (red closer to limiter)

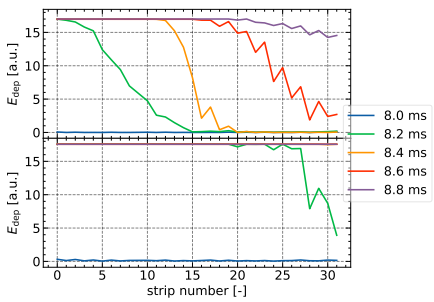

(b) Profiles of the first part of the discharge. Second detector saturated

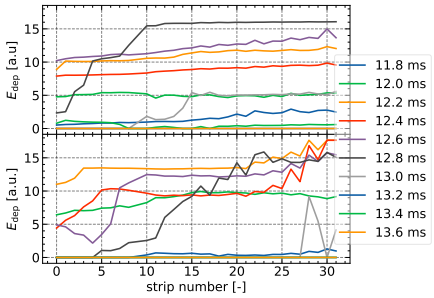

(c) Profiles of later in the discharge. The shift of measured signal to greater distances from plasma (bigger strip no.) propably due to RE drifts

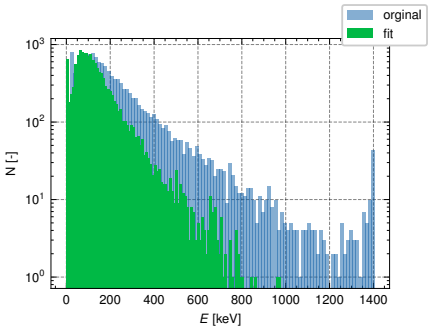

(d) The energetic spectrum of RE reconstructed from LYSO waveform.

Figure 8.8: Shot #38514. B_t, E_t anticlockwise. Detector at limiter edge $d_{lim} \approx 0\,mm$. Energy measurements from two strip detectors in limiter shadow ($d_{limiter} = 8\,mm$) and reconstructed HXR spectra from LYSO waveform. Upper plot show data from detector oriented in the opposite direction in plasma current, lower plot – detector in the direction of plasma current.

17-31, the signal seems to be uniform. This could indicate the presence of backscattered REs.

Shot #38290

Figures 8.10 show measurements from the second discharge performed with the same parameters but toroidal magnetic field and plasma current in an anticlockwise direction. As in the previous case, the data from the detector oriented in the opposite direction to the plasma current facing the REs is plotted on the upper part of the figure. Unlike the previous case, the recorded deposited energy seems more uniform in space. No information about backscattering can be deduced from these data.

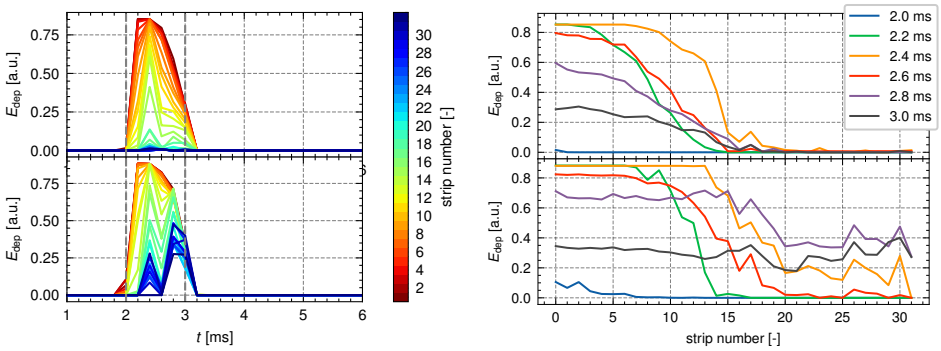

(a) Deposited energy measurements as a function of time. Every line represent on strip of a detector – strip number color coded.

(b) selected energy measurements from figure 8.9(a) as a function of strip number (i.e. distance from limiter); strip number 0 closest to plasma center.

Figure 8.9: Shot #38289. B_t, E_t clockwise. Energy measurements from two strip detectors in limiter shadow ($d_{\text{limiter}} = 8\,\text{mm}$). Upper plot show data from detector oriented in the opposite direction in plasma current, lower plot – detector in the direction of plasma current.

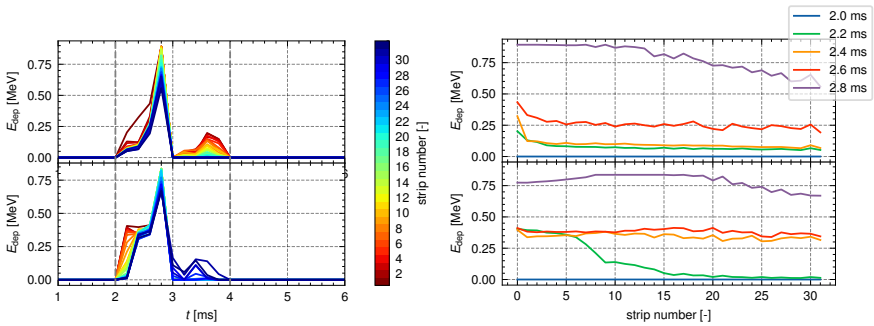

(a) Data from discharge. Each line represent data from one strip. Strip number color coded.

(b) Profiles of deposited energy

Figure 8.10: Shot #38290, B_t, E_t anticlockwise.Energy measurements from two strip detectors in limiter shadow ($d_{\text{limiter}} = 8\,\text{mm}$). Upper plot show data from detector oriented in the opposite direction in plasma current, lower plot – detector in the direction of plasma current.

Shot #38503

Figures 8.11 presents data from discharge # 38503. The discharge was performed with $B_t$and I_p in clockwise direction. The detector was placed $d = 10\,\mathrm{m}m$ from limiter. From HXR data and strip response two stages of RE can be distinguished. At the beginning of discharge, the REs have smaller energies and after about 6.5 ms a number and energy of REs increases. Also, their spatial distribution registered by the strip detector is different. In the first stage,8.11(b) the distribution of REs is in contrary to the prediction of Geant4 simulations. In the later stages, the spatial distribution is more uniform.

Shot #38509

The figurses 8.12 shows results from discharge # 38509, performed with B_t and I_p in clockwise direction. The strip detector was placed further from the limiter, at a distance $d = 10\,\mathrm{mm}$. Profiles with fixed time are plotted in three ranges, as indicated by vertical grey lines in figure 8.12(a). Data from 9.2 ms shown in figure 8.12(b) have similar shapes. There is no distinction between direct REs and backscattered ones. In timestamps 8.4-8.8 ms, there is practically no uniform signal in the second detector, indicating a low number of backscattered REs recorded. The signal from the edge of the sensor is clear in both detectors. Again, the cross-talk between detectors is significant even though the reconstructed spectrum from LYSO indicates that the energy of REs was around 400 keV.

Shot #38952

Figures 8.13 show results from shot #38952, performed with strip detector hidden in the port. Even though the detector should not register any incoming REs, some energy is deposited in the sensor. This could be HXR radiation or electron produced by Compton scattering on detectors cover.

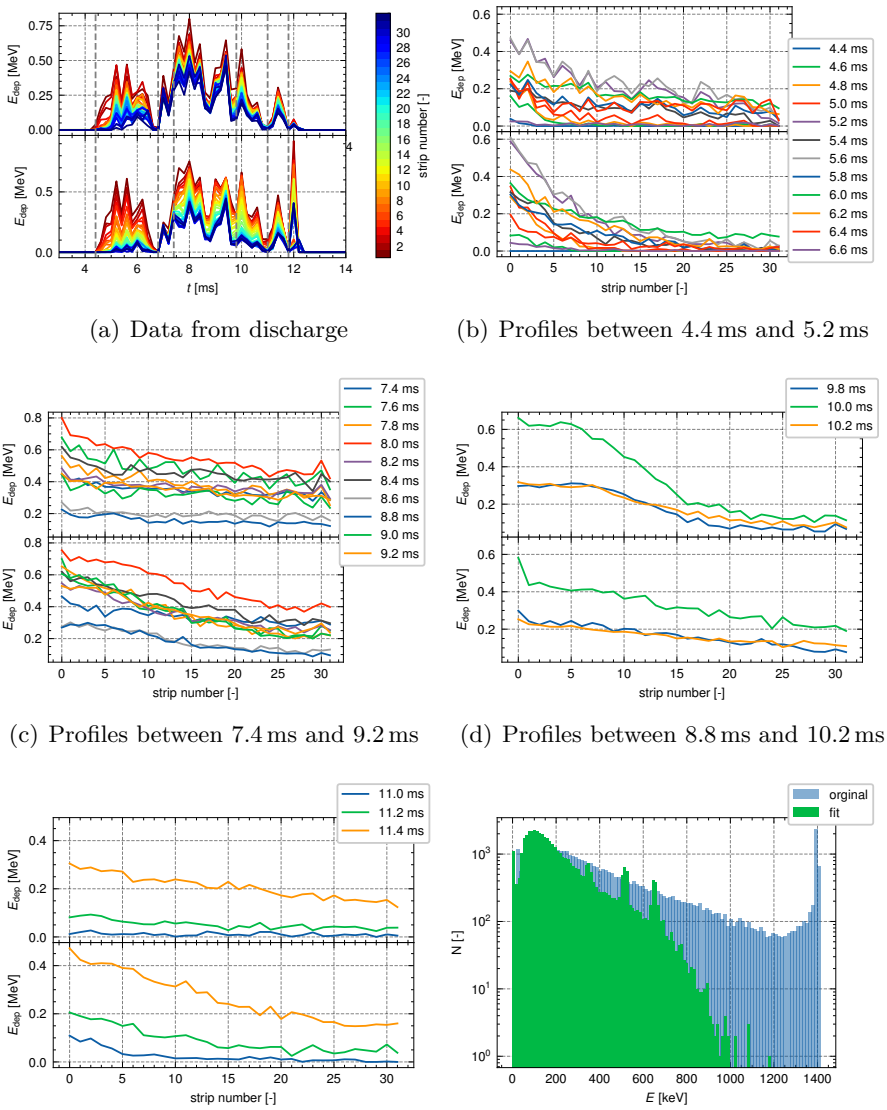

(a) Data from discharge

(b) Profiles between 4.4 ms and 5.2 ms

(c) Profiles between 7.4 ms and 9.2 ms

(d) Profiles between 8.8 ms and 10.2 ms

(e) Profiles between 11.2 ms and 14.4 ms

(f) HXR spectrum from LYSO.

Figure 8.11: Shot #38503 B_t, E_t clockwise. PH32 detectors in limiter shadow ($d_{\text{limiter}} = 10\,\text{mm}$). The LYSO waveform was clipped by an oscilloscope. The two peaks of the reconstructed spectra are artifacts from the fitting algorithm.

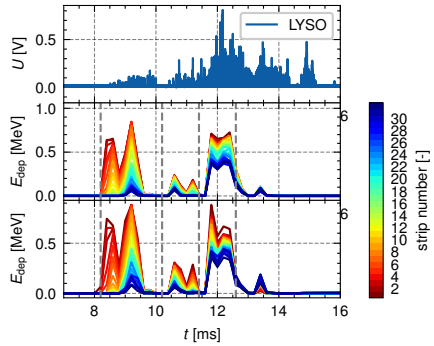

(a) Data from discharge

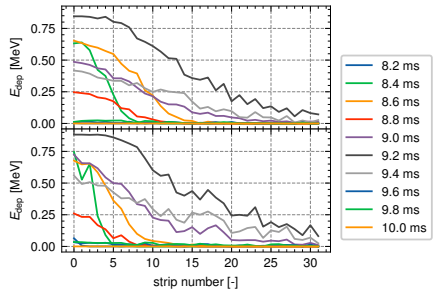

(b) Profiles between 8.2 ms and 10.0 ms

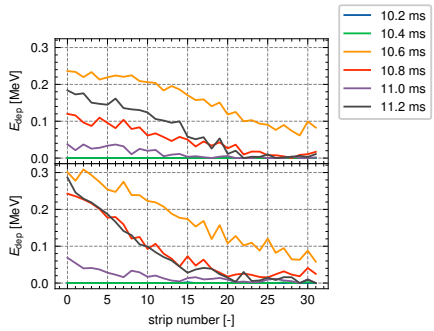

(c) Profiles between 10.2 ms and 11.2 ms

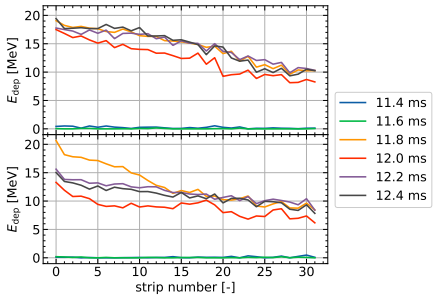

(d) Profiles between 10.4 ms and 11.2 ms

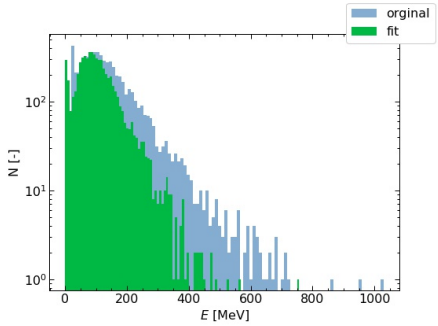

(e) HXR spectrum from LYSO

Figure 8.12: Shot #38509 B_t, E_t anticlockwise. Energy measurements from two strip detectors in limiter shadow ($d_{\text{limiter}} = 10\,\text{mm}$) and reconstructed spectrum of HXR obtained from LYSO waveform. Upper plot show data from detector oriented in the opposite direction in plasma current, lower plot – detector in the direction of plasma current.

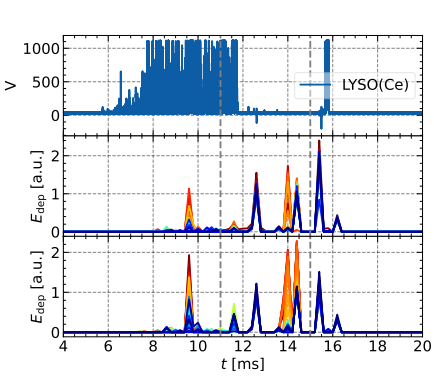

(a) Data from discharge

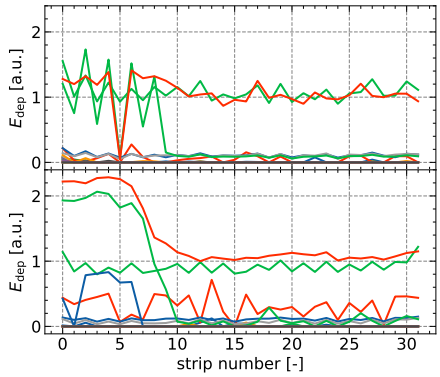

(b) Profiles between 10.4 ms and 14.2 ms

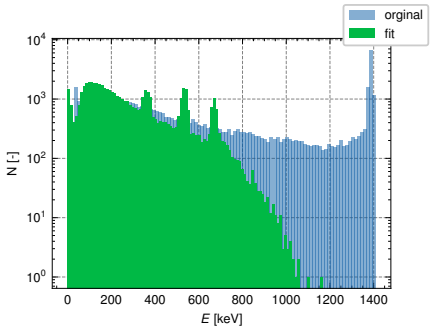

(c) Reconstructed HXR spectra, waveform clipped by oscillscope, the reconstruciton is unreliable

Figure 8.13: Discharge #38952, B_t, E_t clockwise. Strip detectors hidden in port ($d_{\text{limiter}} = 18\,\text{mm}$). Energy measurements from two strip detectors in limiter shadow ($d_{\text{limiter}} = 8\,\text{mm}$) and waveform from HXR detector. Upper plot show data from detector oriented in the opposite direction in plasma current, lower plot – detector in the direction of plasma current. Even when the detector is hidden in the port as small energy is registered

Conclusion

This work summarizes the basics of thermonuclear fusion, plasma physics, and tokamaks. Mechanisms of RE formation, their diagnostics, and mitigation strategies are described. Interactions of electrons and energetic photons with matter relevant for RE diagnostics is also described. Semiconductor and scintillation detectors and their principles of operation are summarized. Finally, the Geant4 simulation toolkit was presented.

A simple model of the tokamak vacuum vessel with limiter and strip detector was constructed. These models were used in Geant4 simulations firstly to evaluate the effect of RE backscattering from the poloidal limiter in GOLEM tokamak and secondly to help the development of strip semiconductor detector setup and to help with interpretation of future measurements with this detector.

The simulation shows that the backscattering of REs from the poloidal limiter should be present and at least 40 % of REs with energies in the range from 100-500 keV impacting the limiter are backscattered.

A new diagnostic tool, composed of two strip semiconductor detectors, was developed to investigate this effect. The results of the measurements at the GOLEM tokamak were compared with Geant4 simulations. Measurements with the strip detector partially support the existence of RE backscattering, but the interpretation of measured data is not clear and further investigation on this topic is required.

Furthermore, a scintillation LYSO crystal coupled to a silicon photomultiplier was added to the HXR diagnostics of the tokamak. The peak clustering was still present in measured waveforms, but due to the good temporal resolution and the high signal-to-noise ratio it was possible to fit the peaks, reconstruct their original height, and thus obtain the HXR spectrum generated by the REs.

The use of a LYSO crystal together with a silicon photomultiplier was found to be a highly suitable diagnostic for HXR generated by REs. The signal quality is even better than one obtained from $CeBr_3$ which has a faster decay time but it is coupled with classical PMT which probably degrades its performance.

The LYSO HXR probe provided information on the maximum energy of REs generated in discharges in GOLEM tokamak. This value was previously

estimated or obtainable only in specific conditions. The method of peak height reconstruction will be added to the HXR diagnostics analysis at the GOLEM tokamak. In the future, a more thorough deconvolution method could be used to obtain the spectra. A silicon strip detector diagnostic tool using two perpendicular sensors has been developed and successfully operated inside a tokamak vessel. Due to the harsh electromagnetic and radiation environment inside the vacuum vessel during discharge, data are not trivial to interpret and the acquired operational experience will be used for further improvement of instruments for direct in-vacuo detection of REs. In particular, a better shielding should be developed to limit the flux of scattered electrons.

Bibliography

[1] S. E. Arthur *et al.*, "The internal constitution of the stars," 1926.

[2] G. M. McCracken, G. McCracken, and P. Stott, *Fusion: the energy of the universe*. Academic Press, 2005.

[3] P. Svihra, D. Bren, A. Casolari, J. Cerovsky, P. Dhyani, M. Farnik, O. Ficker, M. Havranek, M. Hejtmanek, Z. Janoska, *et al.*, "Runaway electrons diagnostics using segmented semiconductor detectors," *Fusion Engineering and Design*, vol. 146, pp. 316–319, 2019.

[4] L. Novotny, J. Cerovsky, P. Dhyani, O. Ficker, M. Havranek, M. Hejtmanek, Z. Janoska, V. Kafka, S. Kulkov, M. Marcisovska, *et al.*, "Runaway electron diagnostics using silicon strip detector," *Journal of Instrumentation*, vol. 15, no. 07, p. C07015, 2020.

[5] J. Wesson and D. J. Campbell, *Tokamaks*, vol. 149. Oxford university press, 2011.

[6] F. F. Chen, *Introduction to plasma physics*. Springer Science & Business Media, 2012.

[7] H. Qin, S. Zhang, J. Xiao, J. Liu, Y. Sun, and W. M. Tang, "Why is boris algorithm so good?," *Physics of Plasmas*, vol. 20, no. 8, p. 084503, 2013.

[8] P. Paruta, P. Ricci, F. Riva, C. Wersal, C. Beadle, and B. Frei, "Simulation of plasma turbulence in the periphery of diverted tokamak by using the gbs code," *Physics of Plasmas*, vol. 25, no. 11, p. 112301, 2018.

[9] M. Kocan, *Ion tempeture measurements in the scrape-off layer of the Tore Supra Tokamak*. PhD thesis, Université Henri Poincaré-Nancy 1, 2009.

[10] "`http://golem.fjfi.cvut.cz/wiki/`."

[11] O. Ficker, "Generation, Losses and Detection of Runaway electrons in tokamaks," 2015.

[12] V. Svoboda, B. Huang, J. Mlynář, G. Pokol, J. Stöckel, and G. Vondrášek, "Multi-mode remote participation on the golem tokamak," *Fusion Engineering and Design*, vol. 86, no. 6-8, pp. 1310–1314, 2011.

[13] C. T. Wilson, "The acceleration of β-particles in strong electric fields such as those of thunderclouds," in *Mathematical Proceedings of the Cambridge Philosophical Society*, vol. 22, pp. 534–538, Cambridge University Press, 1925.

[14] N. J. Fisch, "Theory of current drive in plasmas," *Reviews of Modern Physics*, vol. 59, no. 1, p. 175, 1987.

[15] H. Dreicer, "Electron and ion runaway in a fully ionized gas. i," *Physical Review*, vol. 115, no. 2, p. 238, 1959.

[16] M. D. Kruskal and I. B. Bernstein, "Runaway electrons in an ideal lorentz plasma," *The Physics of Fluids*, vol. 7, no. 3, pp. 407–418, 1964.

[17] J. W. Connor and R. J. Hastie, "Relativistic Limitations on Runaway Electrons," *Nuclear Fusion*, vol. 15, no. 3, pp. 415–423, 1975.

[18] B. N. Breizman, P. Aleynikov, E. M. Hollmann, and M. Lehnen, "Physics of runaway electrons in tokamaks," *Nuclear Fusion*, vol. 59, no. 8, p. 083001, 2019.

[19] A. H. Boozer, "Pivotal issues on relativistic electrons in iter," *Nuclear Fusion*, vol. 58, no. 3, p. 036006, 2018.

[20] R. S. Granetz, B. Esposito, J. Kim, R. Koslowski, M. Lehnen, J. Martin-Solis, C. Paz-Soldan, T. Rhee, J. Wesley, L. Zeng, *et al.*, "An itpa joint experiment to study runaway electron generation and suppression," *Physics of plasmas*, vol. 21, no. 7, p. 072506, 2014.

[21] H. Knoepfel and D. Spong, "Runaway electrons in toroidal discharges," *Nuclear Fusion*, vol. 19, no. 6, p. 785, 1979.

[22] Y. Gribov, D. Humphreys, K. Kajiwara, E. A. Lazarus, J. B. Lister, T. Ozeki, A. Portone, M. Shimada, A. C. Sips, and J. C. Wesley, "Chapter 8: Plasma operation and control," *Nuclear Fusion*, vol. 47, no. 6, pp. S385—-S403, 2007.

[23] M. Lehnen, S. Bozhenkov, S. Abdullaev, M. Jakubowski, T. team, *et al.*, "Suppression of runaway electrons by resonant magnetic perturbations in textor disruptions," *Physical review letters*, vol. 100, no. 25, p. 255003, 2008.

[24] R. Jaspers, "Relativistic runaway electrons in tokamak plasmas," tech. rep., Technische Univ. Eindhoven (Netherlands), 1995.

[25] X. Guan, H. Qin, and N. J. Fisch, "Phase-space dynamics of runaway electrons in tokamaks," *Physics of Plasmas*, vol. 17, no. 9, p. 092502, 2010.

[26] M. Bakhtiari, G. J. Kramer, and D. G. Whyte, "Momentum-space study of the effect of bremsstrahlung radiation on the energy of runaway electrons in tokamaks," *Physics of plasmas*, vol. 12, no. 10, p. 102503, 2005.

[27] A. Russo, "Effect of ripple on runaway electrons in tokamaks," *Nuclear Fusion*, vol. 31, pp. 117–126, jan 1991.

[28] M. Xiao, R. Zhou, L. Hu, Y. Zhang, and E. Team, "Analysis of synchrotron radiation spectra of runaway electrons in tokamak," *Physics of Plasmas*, vol. 24, no. 12, p. 124504, 2017.

[29] A. Cohen and K. Koral, "Empirical equations for electron backscattering coefficients," Tech. Rep. NASA-TN-D-2909, NASA, 07 1965.

[30] H. BOLT, H. CALÉN, and A. MOERTSELL, "Analysis of interaction of disruption induced runaway electrons with plasma facing components in next generation tokamaks," *Journal of Nuclear Science and Technology*, vol. 28, no. 9, pp. 806–813, 1991.

[31] G. F. Knoll, *Radiation detection and measurement*. New York: Wiley, 3rd ed ed., 2000.

[32] G. Lutz, *Semiconductor radiation detectors : device physics*. Berlin New York: Springer, 2007.

[33] Z. Janoška, "Readout electronics of particle detection systems," 2020.

[34] Z. Janoska, M. Carna, M. Havranek, M. Hejtmanek, V. Kafka, M. Marcisovsky, G. Neue, L. Tomasek, and V. Vrba, "Measurement of ionizing particles by the ph32 chip," in *2015 IEEE Nuclear Science Symposium and Medical Imaging Conference (NSS/MIC)*, pp. 1–5, IEEE, 2015.

[35] Z. Janoska, T. Benka, M. Havranek, M. Hejtmanek, J. Jakovenko, V. Kafka, M. Kaschner, M. Marcisovska, M. Marcisovsky, G. Neue, *et al.*, "Time of flight measurements with the ph32 chip," *Journal of Instrumentation*, vol. 14, no. 04, p. C04004, 2019.

[36] Saint-Gobain Crystals, *LYSO Scintillation Material*, 2022.

[37] Saint-Gobain Crystals, *Lanthanum Bromide and Enhanced Lanthanum Bromide*, 2018.

[38] AdvaTech, *CeBr3 - Cerium Bromide Scintillator Crystal*, 2022.

[39] `https://commons.wikimedia.org/wiki/File:PhotoMultiplierTubeAndScintillator.svg`, "Photomultiplier tube and scintillator." Accessed 2020-09-01.

[40] "Sipm working principle - ketek gmbh." Accessed 2020-09-01.

[41] S. Agostinelli, J. Allison, K. a. Amako, J. Apostolakis, H. Araujo, P. Arce, M. Asai, D. Axen, S. Banerjee, G. Barrand, *et al.*, "Geant4—a simulation toolkit," *Nuclear instruments and methods in physics research section A: Accelerators, Spectrometers, Detectors and Associated Equipment*, vol. 506, no. 3, pp. 250–303, 2003.

[42] S. Boogert, A. Abramov, J. Albrecht, G. L. D'Alessandro, L. Nevay, W. Shields, S. Walker, *et al.*, "Pyg4ometry: A tool to create geometries for geant4, bdsim, g4beamline and fluka for particle loss and energy deposit studies," in *10th Int. Particle Accelerator Conf.(IPAC'19), Melbourne, Australia*, 2019.

[43] D. J. Van der Laan, D. R. Schaart, M. C. Maas, F. J. Beekman, P. Bruyndonckx, and C. W. van Eijk, "Optical simulation of monolithic scintillator detectors using gate/geant4," *Physics in Medicine & Biology*, vol. 55, no. 6, p. 1659, 2010.

[44] M. Lé-Magda, E. Dargent, B. Youssef, A. Guillet, J. Idrac, and J.-M. Saiter, "Thermal properties evolution of pcb fr4 epoxy composites for mechatronic during very long ageing," in *Macromolecular Symposia*, vol. 315, pp. 143–151, Wiley Online Library, 2012.

[45] M. Tunkl, "Vývoj nové diagnostiky ubíhajícíh elektronů na bázi křemýkových stripových detektorů," 2019.

[46] A. Kolínksá, "Měření energií ubíhajících elektronů na tokamaku golem."

[47] V. Linhart, D. Bren, A. Casolari, J. Čeřovskỳ, M. Farník, O. Ficker, M. Hetflejš, M. Hron, J. Jakbek, P. Kulhánek, *et al.*, "First measurement of x-rays generated by runaway electrons in tokamaks using a timepix3 device with 1 mm thick silicon sensor," in *2018 IEEE Nuclear Science Symposium and Medical Imaging Conference Proceedings (NSS/MIC)*, pp. 1–9, IEEE, 2018.

Acronyms

ASIC	Application Specific Integrated Circuit 28
CSA	Charge-Sensitive Amplifier) 29, 30
EFIT	Equilibrium Fitting 10
FNSPE	Faculty of Nuclear Sciences and Physical Engineering 1
GDML	Geometry Description Markup Language) 38
Geant4	GEometry ANd Tracking 2, 37, 38, 43, 44, 48, 57
HFS	High-Field Side 8, 11
HXR	Hard X-ray vii, viii, 2, 44, 46–48, 52–54, 57, 58
ICF	Inertial Confinement Fusion 4
LCFS	Last Closed Flux Surface 9, 10
LFS	Low-Field Side 8, 11, 17
LYSO	Lutetium Yttrium Orthosilicate 2, 33, 35, 44, 48–50, 52–54, 57
MCF	Magnetic Confinement Fusion 4
PFC	Plasma Facing Comonent 8
PMT	Photomultiplier Tube 2, 33, 34, 36
RE	Runaway electron vii, viii, 1, 2, 14, 16–19, 22, 38, 40, 41, 43–50, 52, 57, 58
SiPM	Silicon Photomultiplier 2
SOL	Scrape-Off Layer 10

SURE Simple USB Readout Equipment 29